# QCD Studies in *ep* Collisions

Wesley H. Smith*

Physics Department

University of Wisconsin, Madison, WI 53706 USA

## ABSTRACT

These lectures describe QCD physics studies over the period 1992–1996 from data taken with collisions of 27 GeV electrons and positrons with 820 GeV protons at the HERA collider at DESY by the two general-purpose detectors H1 and ZEUS.

The focus of these lectures is on structure functions and jet production in deep inelastic scattering, photoproduction, and diffraction. The topics covered start with a general introduction to HERA and *ep* scattering. Structure functions are discussed. This includes the parton model, scaling violation, and the extraction of $F_2$, which is used to determine the gluon momentum distribution. Both low and high $Q^2$ regimes are discussed. The low $Q^2$ transition from perturbative QCD to soft hadronic physics is examined.

Jet production in deep inelastic scattering to measure $\alpha_s$, and in photoproduction to study resolved and direct photoproduction, is also presented. This is followed by a discussion of diffraction that begins with a general introduction to diffraction in hadronic collisions and its relation to *ep* collisions, and moves on to deep inelastic scattering, where the structure of diffractive exchange is studied, and in photoproduction, where dijet production provides insights into the structure of the Pomeron.

---

# 1. Introduction

The H1 and ZEUS experiments at the HERA *ep* collider, located in the DESY Laboratory in Hamburg, Germany, observe interactions of 27 GeV electrons with 820 GeV protons. The study of electron-proton collisions at HERA is but the most recent in a long and productive series of investigations begun at Stanford by R. Hofstadter in the '50s. The results obtained in *t*-channel (momentum transfer) investigations have provided much of our present knowledge of the structure of the nucleon as well as several fundamental discoveries. Among the milestones are:

*(i)* Proton and neutron form factors. The measurement of the dipole form factor led to the search and discovery of the $\rho$, $\omega$, *etc.*

*(ii)* The two-neutrino experiment, which established lepton flavors.

*(iii)* Bjorken scaling, an entirely experimental discovery, which gave reality to the hitherto imaginary quarks which had been used empirically to successfully classify the resonances.

*(iv)* Measurement of the properties of the quark constituents. The experimental verification of the number, charge, spin, and momentum of the constituents established their identification as quarks and predicted the existence of the gluon.

*(v)* Discovery of prompt leptons produced in neutrino interactions indicating the production of a new quantum number by the weak interaction.

*(vi)* Discovery of the neutral weak current in neutrino-nucleon collisions.

Two recent important milestones from the H1 and ZEUS experiments at DESY are:

*(vii)* Observation of the strong rise of the structure $F_2$ with decreasing *x*, attributed to a singular gluon momentum distribution in the proton at low *x*.

*(viii)* Observation of deep inelastic scattering events characterized by a "large rapidity gap," attributed to diffractive scattering of the virtual photon from proton, proceeding through the exchange of a Pomeron. The study of these events yields information on the flux of Pomerons in the proton and the structure of the Pomeron itself.

The size of a target feature that can be distinguished in the scattering process is inversely proportional to the square of the four-momentum, $Q^2$, transferred to the object being probed. Thus the ability to resolve smaller features requires higher momentum transfers. The construction of the first *ep* collider (HERA) provides a window to this physics at center-of-mass energies of 300 GeV, as compared to 30 GeV reached in fixed-target experiments. This has brought about a new era in the physics of lepton-nucleon scattering, in which both $Q^2$ and energy transfer $\nu$ are increased by two orders of magnitude (equivalent to a fixed-target experiment with a 52 TeV lepton beam). Viewing the collisions at HERA in the Breit Frame, where the quark reverses upon impact with the virtual photon or boson, the interactions resemble those found in $e^+e^-$ colliders, but with energies greater than LEP200.

## 1.1. HERA Data

The HERA collider was commissioned with the first *ep* collisions in the Fall of 1991. First luminosity was observed in the H1 and ZEUS detectors at the end of May 1992 with 26.7 GeV electrons and 820 GeV protons. Since then, there have been four successful data runs, in the summer and the fall of 1992, from June to November 1993, from May to November 1994, and from May to December of 1995. Another run began in July 1996 and is scheduled for completion in December. H1 and ZEUS have had similar data exposures. The '92 summer and fall runs collected about 27 $nb^{-1}$, and the '93 run about 550 $nb^{-1}$. During 1994, ZEUS collected about 800 $nb^{-1}$ with electrons. HERA then switched to running with positrons to increase the luminosity and ZEUS collected about 4.5 $pb^{-1}$. In 1995, ZEUS collected more than 7 $pb^{-1}$ of luminosity with positrons.

# 2. Deep Inelastic Scattering

Deep inelastic scattering (DIS) at HERA typically involves the exchange of a virtual photon as shown in Figure 1. The kinematic variables are defined as:

$$s = (k + P)^2 = \text{center-of-mass energy}$$
$$Q^2 = -q^2 = -(k-k')^2 = (\text{momentum transferred})^2$$
$$x = \frac{Q^2}{2P \cdot q}, \; y = \frac{P \cdot q}{P \cdot k}, \; Q^2 = sxy,$$

where *x* is the fraction of the proton's momentum carried by the struck quark and *y* is the fraction of the electron's energy lost in the proton rest frame. The topology of a DIS event is shown in Figure 2, illustrated with a ZEUS event in Figure 3. The electron

and the current jet from the struck quark are observed in the central detector, while the proton remnant travels unobserved down the forward beampipe in the proton direction.
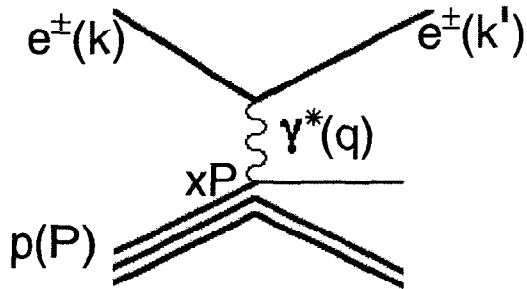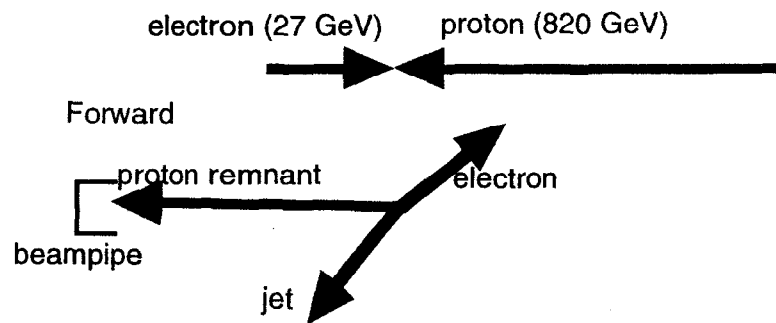


Figure 1. A deep inelastic scattering event.



Figure 2. Topology of a deep inelastic scattering event at HERA.

The reconstruction of the $x$ and $Q^2$ of DIS events is determined from the energy and angle of the scattered electron ($E_e'$, $\theta_e'$) and the energy and angle of the current jet ($E_h$, $\gamma_h$). Only two of these four measured quantities are required to reconstruct $x$ and $Q^2$. For example, in terms of the scattered electron energy and angle ($E_e'$, $\theta_e'$), we have:

$$Q^2 = 4 E_e E_e' \cos^2 \frac{\theta}{2}, \quad x = \frac{E_e \cos^2 \frac{\theta}{2}}{E_p \left[ 1 - \frac{E_e'}{E_e} \right]}, \quad y = 1 - \frac{E_e'}{E_e} \sin^2 \frac{\theta}{2}.$$

The reconstruction methods using various combinations of the variables $E_e'$, $\theta_e'$, $E_h$, and $\gamma_h$ have different responses to detector effects and vary in accuracy for different kinematic regions. The optimal reconstruction method, called the $P_T$ method, provides the best performance for the full kinematic range using all four variables, conservation of $E - P_z$ (see Sec. 2.1.1), and $P_T$ balance between the electron and current jets.
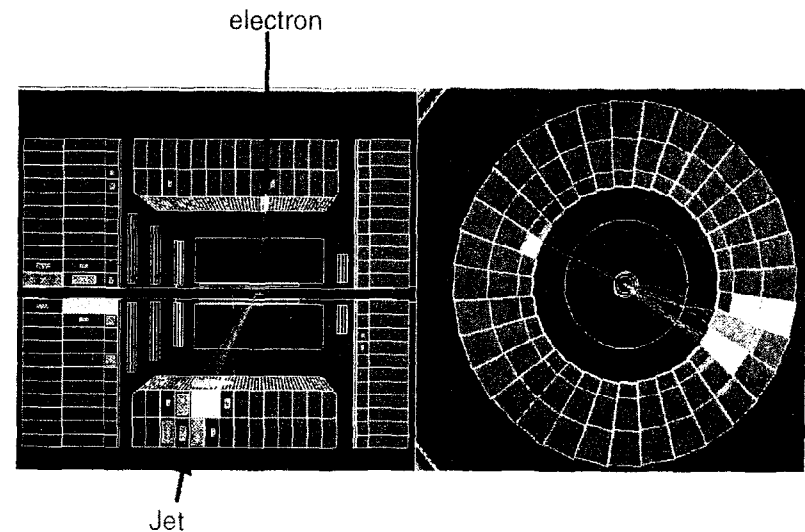


Figure 3. A deep inelastic scattering event observed in ZEUS with $Q^2 = 1600$ GeV$^2$.

## 2.1. Backgrounds

### 2.1.1. Photoproduction

Photoproduction is not only a large source of background to DIS events, especially at high $y$, but also is the source of many interesting physics results that will be discussed in Sec. 2.3.3. Photoproduction in $ep$ scattering occurs when the electron is scattered at very small angles ($\theta < 1.0°$) and $Q^2$ is very close to zero ($Q^2 < 0.2$ GeV$^2$). Since the

outgoing electron in photoproduction events is emitted at very low angles, in most cases it escapes undetected down the beampipe in the electron direction. However, even though the outgoing electron is missing, some photoproduction events can contaminate the DIS sample through false identification of hadronic activity as the scattered electron. Since the *ep* interaction cross section via virtual photon exchange is proportional to $1/Q^2$, photoproduction is the dominant source of physics events at HERA, and even a small fraction of contamination from photoproduction events creates a sizable background.

There are several techniques used to suppress the photoproduction background. If the falsely identified electron is caused by a deposit of hadronic energy near the forward beampipe, the event will have a large reconstructed $y$, which can be removed by a $y$ cut. We can also use conservation of the difference between the energy of the event and the energy in the proton beam direction:

$$(E_{tot} - P_{z\ tot})_{final} = (E_{tot} - P_{z\ tot})_{initial} = (E_p + E_e) - (E_p + E_e) = 2E_e.$$

Since the proton remnant jet contributes very little to this expression due to its small forward angle, we expect the value of $(E_{tot} - P_{z\ tot})$ for DIS events to be $2E_e$. For photoproduction events, the scattered electron of energy $E_e'$ escapes undetected in the electron direction, yielding a lower value of $(E_{tot} - P_{z\ tot}) = 2E_e - E_e'$.

### 2.1.2. Beam-Gas Background

A large source of background comes from interactions of the proton beam with the residual beampipe gas. Events from protons that interact after passing through the detector are not seen. Events from protons that interact before passing through the detector can be eliminated by measurement of the event time. The topology of a typical proton beam-gas interaction is shown in Figure 4. Beam-gas events can create energy deposits that mimic both the scattered electron and the current jet. However, the timing of these events is different than events from the interaction point, which deposit energy in the rear calorimeter (direction of the electron beam) after the proton has traveled to the interaction point and the scattered electron has traveled back to the detector. Beam-gas interactions upstream of the detector directly strike the detector at a time different from the round-trip time of flight from the detector to the interaction point and back, which is about 13 ns.
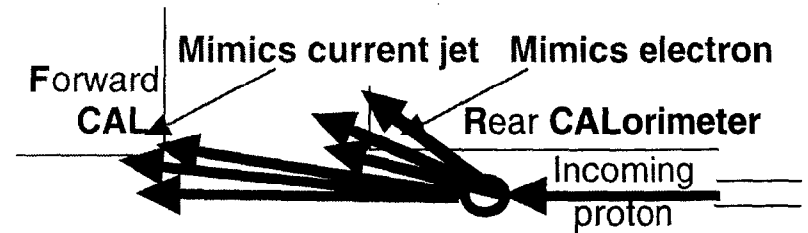


Figure 4. Topology of a typical upstream proton beam-gas interaction.

Proton beam-gas events that originate in the detector can be eliminated with cuts on $(E_{tot} - P_{z\ tot})$ as described in Sec. 2.1.1. The very small background remaining after these cuts and the very small background from electron beam-gas background is calculated from the event rate for special noncolliding bunches of electrons and protons that are not paired with a corresponding proton or electron bunch.

## 2.2. Phenomenology of Deep Inelastic Scattering

### 2.2.1. Deep Inelastic Scattering Cross Section

The neutral current *ep* DIS differential cross section is:

$$\frac{d\sigma^{NC}(e^{\pm}p)}{dxdQ^2} = \frac{2\pi\alpha^2}{xQ^4}Y_+\left[F_2 - \frac{y^2}{Y_+}F_L \mp \frac{Y_-}{Y_+}xF_3\right],$$

where $Y_{\pm} = 1 \pm (1 - y^2)$. The virtual photon is either longitudinally or transversely polarized. The structure function $F_2(x, Q^2)$ gives the interaction between transversely polarized photons and spin-1/2 partons, and equals the charge weighted sum of the quark distributions. The structure function $F_L(x, Q^2)$ gives the cross section due to longitudinally polarized photons that interact with the proton. The partons that interact with these photons need to have high transverse momentum, which happens predominantly at high $y$. The structure function $F_3(x, Q^2)$ is the parity violating structure function which is due to $Z^0$ exchange, which is only an appreciable part of the cross section at high $Q^2$.

### 2.2.2. Parton Model

Beginning in 1967, a series of *ep* scattering experiments at SLAC[1] showed that the DIS cross section fell weakly with increasing $Q^2$ and that the momentum distributions of

the proton constituents (i.e., the structure functions), depended only on $x$. The $Q^2$ independence of the structure functions, called *scaling*, had been predicted by Bjorken[2] and was incorporated by Feynman[3] into the *parton model*, which assumed the proton was composed of non-interacting point-like partons, from which the electron scatters incoherently.

In the parton model, the structure function $F_2$ is given by the charge-weighted sum of the parton momentum densities, $F_2(x) = \sum_i e_i^2 x f_i(x)$. For spin-1/2 partons, $F_L = 0$ and for spin-zero partons, $F_L = F_2$. The parton densities are not calculable in this model and therefore are derived from experiment. DIS provides an excellent laboratory for the extraction of the parton densities because the electromagnetic probe is well-understood.

In the quark-parton model,[4] partons are identified with fractionally charged quarks that come in several flavors. The proton is made of three valence quarks, and a distribution of quark-antiquark pairs called the sea quarks. The singlet and nonsinglet quark flavor combinations are defined as:

$$q^{SI}(x) = \sum_i \left( q_i(x) + \bar{q}_i(x) \right), \qquad q^{NS}(x) = \sum_i \left( q_i(x) - \bar{q}_i(x) \right),$$

where the subscript $i$ runs over all flavors. Under the assumption that $u(x) = u^v(x) + u^s(x)$ and $\bar{u}(x) = u^s(x)$, we have $q^{NS}(x) = u^v(x) + d^v(x)$ where $v$ and $s$ stand for valence and sea, respectively. The measurement of the momentum sum rule, $\int_0^1 x q^{SI}(x) dx < 1$, and its experimental determination[5] as ~0.5, led to acceptance of the addition of the electrically neutral gluons, the field quanta responsible for the binding of the quarks to the proton constituents,[6] i.e., $\int_0^1 \left( x q^{SI}(x) + xg(x) \right) dx = 1$.

Therefore, measurement of the gluon momentum density, $xg(x)$, is required to fully understand the structure of the proton. It is also particularly important at low $x$, where gluon scattering dominated the proton collision cross sections.

### 2.2.3. Perturbative QCD

QCD produces interactions between quarks and gluons which cause the quarks to acquire transverse momentum, which causes scaling violation: $F_2(x) \rightarrow F_2(x, Q^2)$.

Examples of these interactions are shown in Figure 5. The probabilities for these interactions are called splitting functions and have a $\ln(Q^2)$ behavior.
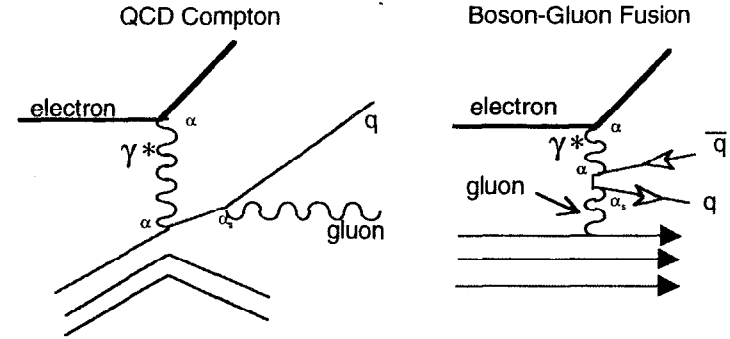


Figure 5. QCD interactions between quarks and gluons.

As $Q^2$ increases, the photon is able to resolve finer structure in the proton and interacts with the cloud of partons (quarks and gluons) around each valence quark that shares the proton's momentum. As $x$ decreases, the fraction of proton momentum needed to be carried by the struck parton decreases, increasing the likelihood that such a parton is present. Therefore, we expect the number of quarks to increase with decreasing $x$, and we expect this effect to be more pronounced at higher $Q^2$. The detailed expectations for these changes are discussed below.

The evolution of the quark and gluon densities of the proton with $Q^2$ and $x$ is given by perturbative QCD. Given an empirical parameterization for the parton densities at some $Q^2 = Q_0^2$: $xg(x) = A_g x^{\delta_g}(1-x)^{\eta_g}(1+\gamma_g x)$, $xq^{NS}(x) = A_{NS} x^{\delta_{NS}}(1-x)^{\eta_{NS}}$, and $xq^{SI}(x) = A_{SI} x^{\delta_{SI}}(1-x)^{\eta_{SI}}(1+\varepsilon_{SI}\sqrt{x}+\gamma_{SI}x)$, the Dokshitzer-Gribov-Lipatov-Altarelli-Parisi (DGLAP)[7] equations describe the evolution of the parton densities to higher $Q^2$:

$$\frac{dq_i(x,Q^2)}{d\ln Q^2} = \frac{\alpha_s(Q^2)}{2\pi} \int_x^1 \frac{dw}{w} \left[ q_i(w,Q^2) P_{qq}\left(\frac{x}{w}\right) + g(w,Q^2) P_{qg}\left(\frac{x}{w}\right) \right]$$

$$\frac{dg(x,Q^2)}{d\ln Q^2} = \frac{\alpha_s(Q^2)}{2\pi} \int_x^1 \frac{dw}{w} \left[ \sum_i q_i(w,Q^2) P_{gq}\left(\frac{x}{w}\right) + g(w,Q^2) P_{gg}\left(\frac{x}{w}\right) \right],$$

where the functions $P_{ij}(x/y)$ are called the splitting functions, which give the probability that a parton (either a quark or a gluon) $i$ with momentum fraction $x$ originated from a parton $j$ with momentum fraction $y$, where $x < y < 1$. The coupling constant $\alpha_s$ of the

strong force is given in lowest order by: $\alpha_s(Q^2) = \dfrac{12\pi}{(33-2n_f)\log(Q^2/\Lambda^2)}$, where $n_f$ is

the number of flavors and $\Lambda$ is a QCD parameter that governs the $Q^2$ dependence, and in particular, sets the boundary for $Q^2 \gg \Lambda^2$ where $\alpha_s$ is sufficiently small to justify a perturbative treatment in terms of quasifree quarks and gluons. The logarithmic radiative QCD processes and their subsequent parton evolution as characterized by the DGLAP equations result in the logarithmic scaling violations that render the structure functions dependent on both $x$ and $Q^2$. Even though the structure function $F_2$ is given by $F_2(x,Q^2) = \sum_i e_i^2 x q_i(x,Q^2)$, since the DGLAP equations couple the quark and gluon distributions, $F_2$ also depends on the gluon distribution as well as the quark distributions. Moreover, since the structure function is extracted from the cross section, and the calculation of the DIS cross section requires $F_L$,

$$F_L(x,Q^2) = \frac{\alpha_s(Q^2)}{\pi} \int_x^1 \frac{dw}{w} \left(\frac{x}{w}\right)^2 \left\{ \frac{4}{3} F_2(w,Q^2) + 2\sum_i e_i^2 \left(1 - \frac{x}{w}\right) w g(w,Q^2) \right\},$$

the parameterization of the gluon density can be determined by fitting QCD evolution to the DIS data.

### 2.2.4. Parton Distribution Functions

Parton Distribution Functions (PDF's) describe the sharing of the proton's momentum amongst its partons (gluons, valence, and sea quarks). Martin, Roberts, and Stirling[8] (MRS) and the Coordinated Theoretical/Experimental Project on QCD[9] (CTEQ) assume $g(x,Q_0^2) \sim x^{\gamma_1}$ and $F_2(x,Q_0^2) \sim x^{\gamma_2}$, where $Q_0^2 = 4\,\text{GeV}^2$, and they evolve in $Q^2$ according to the DGLAP equations, using the single parameterization to produce a global fit to the world DIS data. Glück, Reya, and Vogt[10] (GRV) start with valence-like parton (gluon, valence, and sea quark) distributions at $Q_0^2 = 0.3\,\text{GeV}^2$ and they evolve in $Q^2$ using the DGLAP equations. This dynamically generated growth in the parton distribution functions (PDF's) predicts a rapid rise at low-$x$ with $g(x,Q^2)$ and $F_2(x,Q_0^2) \sim x^\gamma$, where $\gamma \ll -0.08$.

### 2.2.5. Models for Low $Q^2$ and Low $x$

In the low-$Q^2$ region where the proton is mostly sea quarks and gluons, perturbative QCD cannot be used and other models must be used to predict the behavior of the structure functions. One approach is to use Regge theory, which describes hadron-

hadron and real photoproduction cross sections in terms of the exchange of a non-perturbative particle, or "Reggeon" in the $t$-channel. In the limit as $s \to \infty$, only one of these Reggeons survives, the Pomeron. The Pomeron has the quantum numbers of the vacuum. Donnachie and Landshoff[11] (DL) extended the Regge picture to virtual photoproduction cross sections for $Q^2 < 10\,\text{GeV}^2$. This approach assumes that

since : $F_2 = \dfrac{Q^2}{4\pi\alpha^2}\sigma(\gamma^* p)$ but at $Q^2 = 0 : \sigma(\gamma^* p) = C \times (W^2)^{+0.08}$;

and at low $x$ : $W^2 = \dfrac{Q^2}{x} \to \sigma(\gamma^* p) = C'(Q^2)x^{-0.08}$, then : $\displaystyle\lim_{Q^2 \to 0} F_2(x,Q^2) = f(Q^2)x^{-0.08}$.

Therefore, they relate the structure function to Reggeon exchange phenomena which successfully describe the slow rise of total cross sections with center-of-mass energy in hadron-hadron and photoproduction reactions.

In the limit $x \to 0$, the splitting functions become singular and the $\ln(1/x)$ terms become important. The Balitsky, Fadin, Kuraev, and Lipatov[12] (BFKL) equation is a perturbative QCD approach that resums the leading powers of $\ln(1/x)$, producing an evolution equation in $x$. The analytic solution to this equation results in a gluon distribution:

$$g(x,Q_0^2) \sim x^\gamma \text{ and } \gamma = -\frac{12\ln(2)}{\pi}\alpha_s \sim -0.5.$$

The BFKL approach may be viewed as the exchange of many gluons, which corresponds to the same quantum numbers as the Pomeron. This multigluon system is referred to as the BFKL Pomeron. Since this perturbative QCD process is taking place at relatively high $t$, the BFKL Pomeron is called a "hard Pomeron" in contrast to the "soft Pomeron" referred to above in the nonperturbative DL model, which is exchanged at low $t$.

## 2.3. Measurement of $F_2$ and Gluon Extraction

### 2.3.1. Technique and Kinematic Range

The measurement of $F_2$ at HERA starts by binning the data in $x$ and $Q^2$ and subtracting the background. The cross section is multiplied by a QCD calculation of $F_L$ using parameterizations of $q(x, Q^2)$ and $g(x, Q^2)$. The acceptance is measured by a Monte Carlo calculation. $F_2$ is then unfolded iteratively until the Monte Carlo matches the data.

Finally, the systematic errors are estimated by repetition of the analysis with excursions within the error envelope.

The H1 (Ref. 13) and ZEUS[14] $F_2$ data cover a large kinematic range with $Q^2$ from 0.16 to 15,000 GeV$^2$ and $x$ values between 3 x 10$^{-6}$ and 0.8. The experiments have been able to explore the low-$x$, low-$Q^2$ regime through several techniques. Both H1 and ZEUS have taken shifted vertex (SVX) runs with the interaction point moved in the proton direction to give an extended lever arm for electrons striking their rear calorimeters, thereby reducing the acceptance cutoff for low $Q^2$. In addition, both experiments analyzed data with initial state radiation (ISR) from the electron, which reduced the energy of the incoming electron, which also permits access to lower $Q^2$ scattering within the detector acceptance. Finally, ZEUS added a calorimeter behind and between the rear calorimeter and the beampipe. This beampipe calorimeter (BPC) detects electrons scattering at very shallow angles that would otherwise be unobserved.

Figure 6 compares the range of structure function measurements from H1 and ZEUS with deep inelastic fixed target electron scattering at SLAC and muon scattering at CERN (BCDMS,[15] NMC[16]) and Fermilab [E665 (Ref. 17)]. This shows that the HERA experiments have extended the range of both $x$ and $Q^2$ measurements by more than two orders of magnitude. There is also considerable overlap between the HERA results and those of E665 and NMC, providing for comparisons with the fixed target regime.

### 2.3.2. $F_2$ Results

Figure 7 shows the final results for $F_2$ versus $x$ in $Q^2$ bins from the H1 and ZEUS 1994 data sets, along with the fixed target muon scattering experiments BCDMS, NMC, and E665. The dramatic rise in $F_2$ with decreasing $x$ is evident over a wide $Q^2$ range from 1.5 to 5000 GeV$^2$. This rise is attributed to a sharp increase in the gluon content with decreasing $x$ at low values of $x$. This singular gluon behavior is further discussed in Sec. 2.3.3.
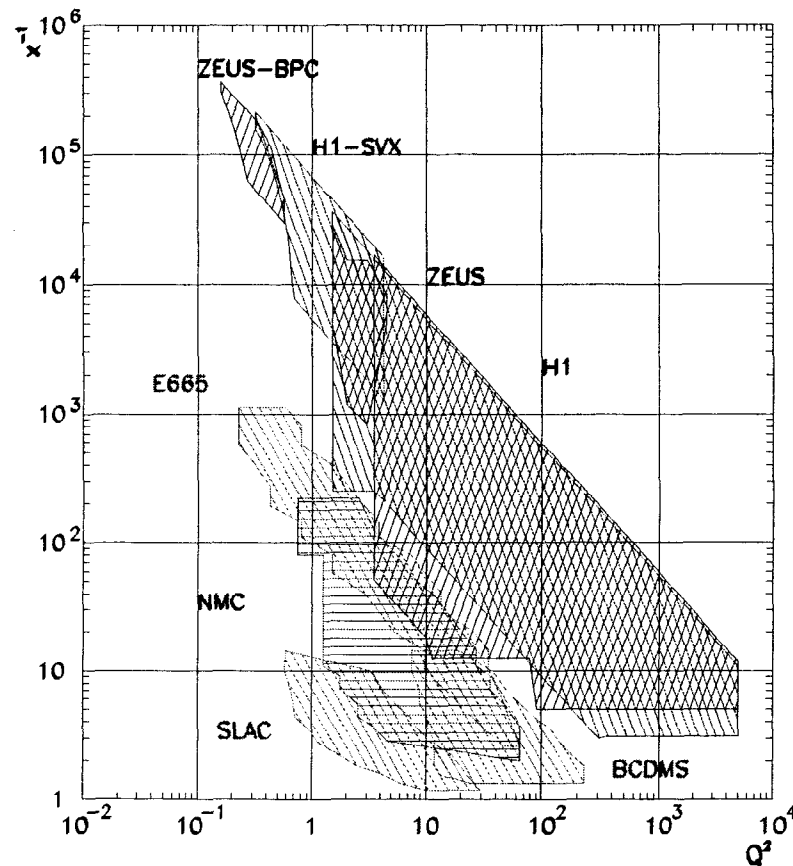


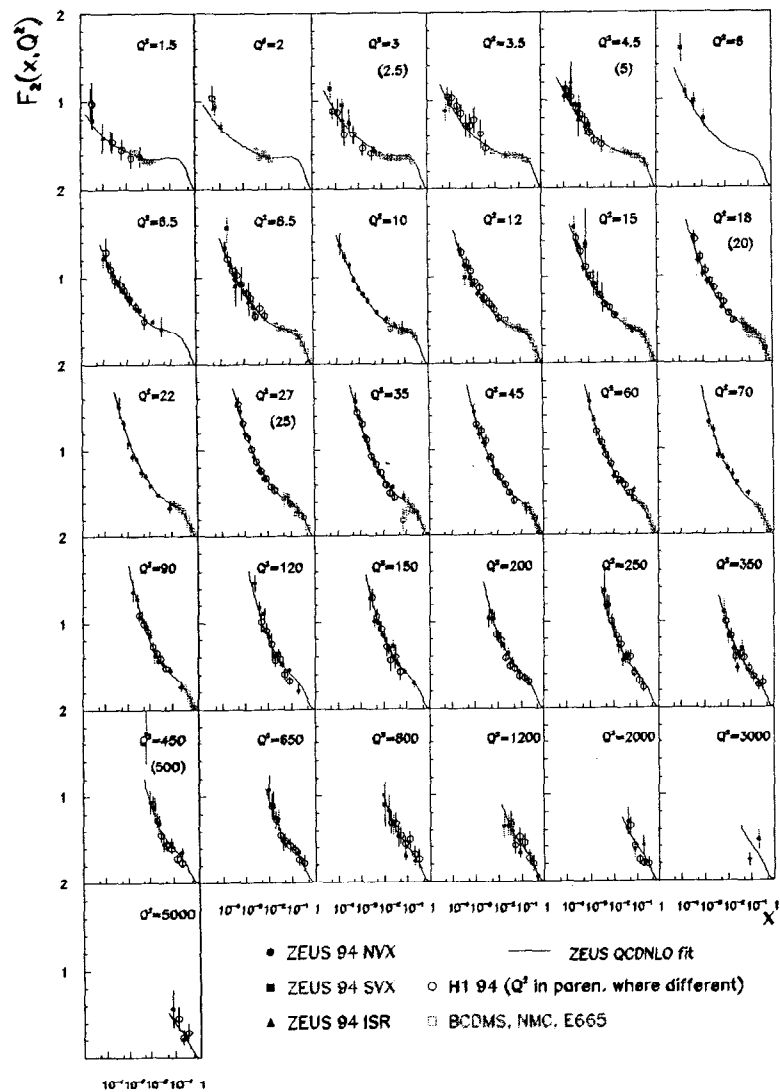Figure 6. Kinematic range of structure function measurements.

Figure 7. Measurements of $F_2$ versus $x$ for various $Q^2$ bins from H1, ZEUS (Normal VerteX, Shifted VerteX, and Initial State Radiation samples), and fixed target muon scattering experiments at CERN (NMC, BCDMS) and Fermilab (E665).

There is good agreement between H1 and ZEUS, as well as between the HERA results and the fixed target muon scattering data of BCDMS, NMC, and E665. Also shown is a next-to-leading order (NLO) QCD fit used for the acceptance calculation for ZEUS. This fit agrees well with the data, showing that the QCD evolution characterized by the DGLAP equations describes that data well down to $x = 3 \times 10^{-5}$. The agreement between the data and the ZEUS QCD NLO fit indicates that the DGLAP evolution approaches of MRS, CTEQ, and GRV are sufficient to explain the data shown in Figure 7 and that it is not necessary to invoke the BFKL equation to resum the $\ln(1/x)$ terms in the kinematic regime covered by the HERA data thus far. Further investigation at low $x$ and low $Q^2$ is discussed in Sec. 2.3.4.

At large $x$ and at $Q^2$ values up to 70 GeV$^2$, where the HERA data reach the $x$ range covered by the fixed-target experiments, good agreement with the muon scattering results is observed. The agreement of the QCD NLO fit with both the HERA and fixed target muon scattering data shows a consistent picture between QCD evolution and the experiments over a wide kinematic range. This observation is further underscored by the good agreement between the HERA data and the latest parton distribution functions from the global data analyses produced by CTEQ[18] and MRS[19].

### 2.3.3. Extraction of the Gluon Density

Figure 8 shows measurements of $F_2$ as a function of $Q^2$ for various bins of $x$ from H1, ZEUS, and fixed target muon scattering experiments at CERN (NMC, BCDMS) and Fermilab (E665). There is good agreement between ZEUS and H1, as well as good agreement between the HERA measurements and the fixed target results where they overlap from $x = 0.004$ through 0.081. The QCD NLO fit is also shown. It agrees well with the HERA and muon scattering data, indicating that the measured $x$-$Q^2$ behavior of $F_2$ is described by QCD using DGLAP evolution over the full kinematic range. The plot also shows the variation of $F_2$ with $Q^2$, showing strong QCD-predicted scaling violations for $x < 0.02$. Since these scaling violations are caused by gluon radiation, they can be used to determine the gluon distribution.

As pointed out in Sec. 2.2.3, the logarithmic slope $dF_2/d\ln Q^2$ provides a measurement of the gluon distribution. An example of the fitting technique can be taken from the ZEUS analysis of the 1994 $F_2$ data. The NMC data was used to constrain the fit at larger values of $x$. The momentum sum rule was used to constrain
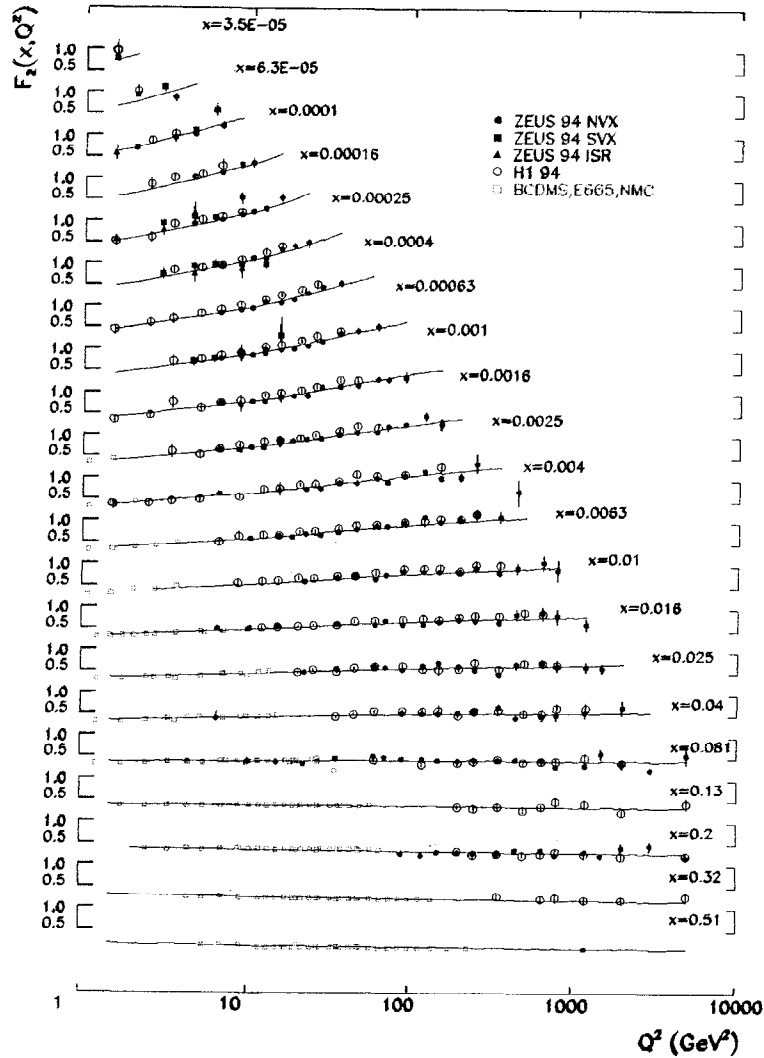
Figure 8. $F_2$ versus $Q^2$ for various bins of x for H1, ZEUS, and for fixed target muon
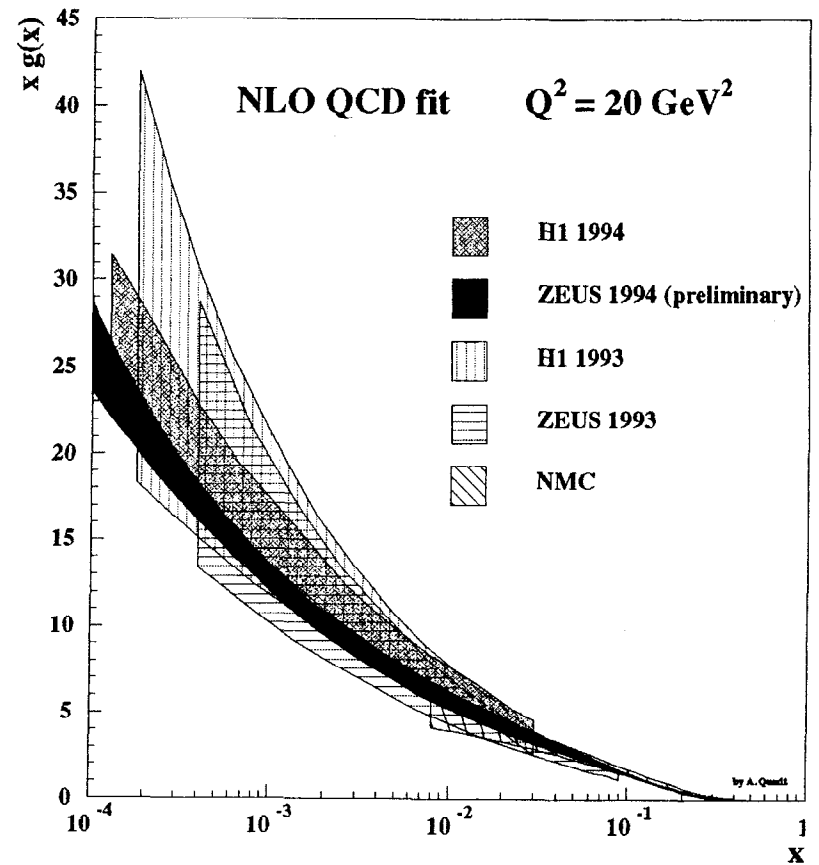scattering (BCDMS, E665, NMC) along with the NLO QCD fit to ZEUS data.



Figure 9. Results for fits to the gluon distribution from H1 and ZEUS from the 1993
and 1994 data sets.

the gluon density. The functional forms of the quark and gluon densities shown in Sec.
2.2.3 were assumed. The SLAC/BCDMS value of $\alpha_s(M_Z^2) = 0.113$ was assumed and
evolved in $Q^2$. The quark and gluon distributions were evolved using the
DGLAP equations to measured $Q^2$ bins to calculate $F_2$, and this was compared to the
data by computing a $\chi^2$ with statistical errors only. A nonlinear minimization of the $\chi^2$
was then used to find the fit parameters of the assumed functional forms of the quark
and gluon distributions. Finally, the systematic uncertainty was estimated separately by
varying each of the 31 different systematic effects individually and performing a new
fit.

Figure 9 shows the results of NLO QCD fits for the gluon density from H1 (Ref. 20), ZEUS,[21] and NMC[16] data for $Q^2 = 20$ GeV$^2$. The most striking effect is the more than an order of magnitude increase in the gluon content of the proton from about one gluon per unit of rapidity to more than 20 for $x$ approaching $10^{-4}$. It is also important to notice the major increase in range from that of the NMC experiment to the HERA results, as well as the significant improvement in the uncertainty and validity range in the kinematic plane between the 1993 and 1994 HERA measurements, while the agreement between the 1993 and 1994 HERA measurements remains quite good. The ZEUS measurement found an exponent of the gluon distribution (see Sec. 2.2.3) $\delta_g = 0.24 \pm 0.02$, and the momentum sum rule at $Q^2 = 7$ GeV$^2$ determined contributions of 0.555 quarks + 0.445 gluons.

There are some general caveats in order, concerning the extraction of $F_2$ and the gluon density. These analyses involve a priori assumptions for $\alpha_s$ and the quark-gluon parameterization in order to compute the $F_L$ and $F_3$ corrections to the DIS cross section. The extracted $F_2$ is sensitive to these assumptions, particularly for the high-$y$ kinematic range data, which is sensitive to the gluon. Therefore, it is more prudent to perform an assumption-independent analysis by directly fitting the cross-section data. The results of such an analysis can yield consistent values for $\alpha_s$ and the quark and gluon parameterizations.

### 2.3.4. Low $Q^2$ Measurements

The use of techniques such as shifted vertex running and initial state radiation analysis, as well as the data from the ZEUS beampipe calorimeter (BPC), have enabled measurements at lower $Q^2$ in the low-$x$ region. This allows the study of the transition between DIS and photoproduction. At $Q^2 = 0$, the dominant processes are non-perturbative and described by Regge theory. As $Q^2$ increases, it is expected to observe the onset of perturbative QCD. The nature of the transition from a soft process of low virtuality to a hard process of high virtuality should provide understanding of both types of interactions. Knowledge of the low $x$ and low $Q^2$ region is also needed for the calculation of radiative corrections.
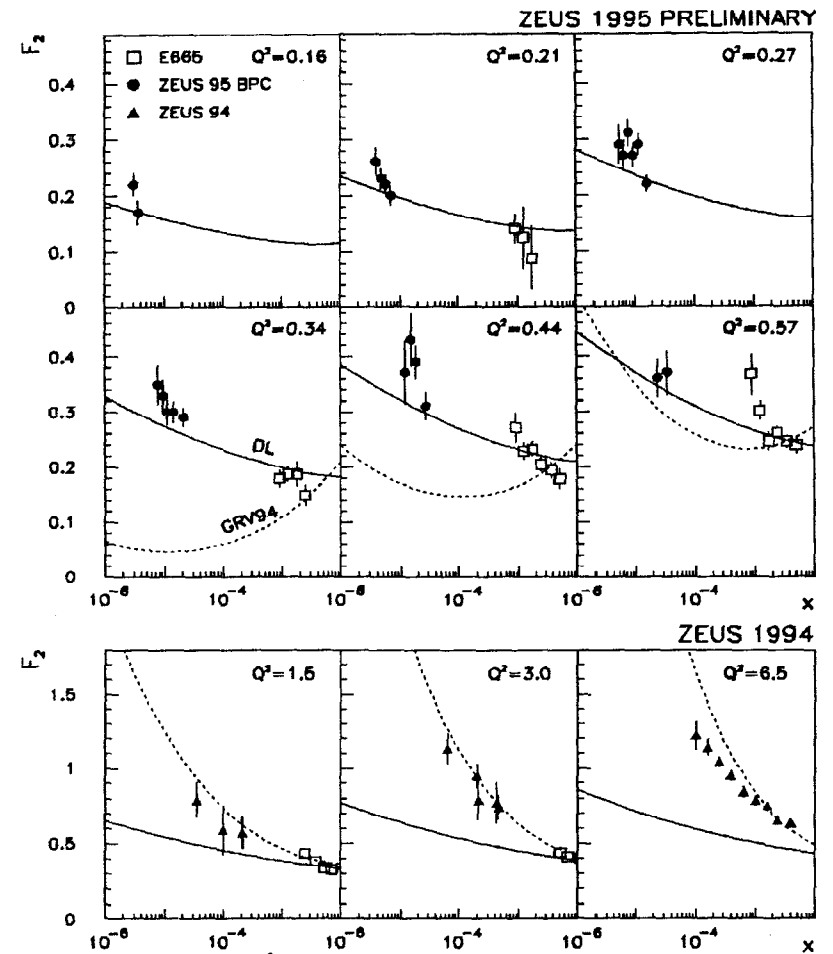


Figure 10. $F_2$ versus $x$ in $Q^2$ bins from the 1995 ZEUS BPC (upper six plots) and 1994 shifted and normal vertex (lower three plots) data shown with E665 muon scattering results at the closest $Q^2$ values. Also shown are the theoretical predictions of GRV (dotted lines) and DL (solid lines).

The top six plots of Fig. 10 show the preliminary ZEUS BPC $F_2$ results for $0.16 \leq Q^2 \leq 0.57$ GeV$^2$. Also shown are the data from the E665 (Ref. 17) measurement at a similar $Q^2$, but much larger $x$. There is a rise in $F_2$ of approximately 1.5 to 2 from $x$ near $10^{-3}$ to $x$ near $10^{-5}$. The bottom of Fig. 10 shows $F_2$ values from ZEUS and E665 for $Q^2 = 1.5$, 3.0, and 6.5 GeV$^2$ showing a rapid rise of $F_2$ as $Q^2$ increases. The rise of $F_2$ over two to three decades in $x$ from E665 to ZEUS for $0.16 \leq Q^2 \leq 0.57$ GeV$^2$ agrees with the expectations of the DL model discussed in Sec. 2.2.5. However, at

higher $Q^2$, the DL prediction falls substantially below the ZEUS result. The GRV perturbative QCD prediction for $F_2$ accounts for about 40% of the measured $F_2$ at $Q^2 =$ 0.44 GeV$^2$ and about 80% at $Q^2 = 0.57$ GeV$^2$. At larger $Q^2$ values, the GRV prediction reproduces the rapid rise of $F_2$, but is somewhat higher. We therefore observe the transition from a region of $Q^2 \leq 0.5$ GeV$^2$, where the DL soft Pomeron model describes almost real photoproduction and the perturbative QCD picture does not describe the measured behavior, to a region of $Q^2 \geq 1.5$ GeV$^2$, where a perturbative QCD prediction is valid and the Regge picture is no longer appropriate.

A useful way to display the results for $F_2$ is to plot the total $\gamma^* p$ cross section using the relation: $\sigma^{\gamma^* p}(W^2, Q^2) = \dfrac{4\pi^2 \alpha}{Q^2} \dfrac{1}{1-x}\left(1 + \dfrac{4M^2 x^2}{Q^2}\right) F_2(x, Q^2)$. Figure 11 shows $\sigma(\gamma^* p)$ as measured by ZEUS[21,22] and E665 (Ref. 17) as a function of $W^2$ for $Q^2$ bins from 0.15 through 6.5 GeV$^2$. The total real photon-proton cross-section measurements from ZEUS[22], H1 (Ref. 23), and fixed-target experiments[24] are also shown. The curves show the DL soft Pomeron model and the GRV perturbative QCD model. As discussed in Sec. 2.2.5, the DL model predicts $\sigma(\gamma^* p) \sim (W^2)^{0.08}$. The GRV model predicts a stronger variation with $Q^2$ and $W^2$. At low $Q^2$, the DL model describes the data well, but fails at $Q^2 \geq 1.5$ GeV$^2$. At $Q^2 \geq 1.5$ GeV$^2$, the GRV prediction agrees with the rapid rise in $\sigma(\gamma^* p)$ with $W^2$ observed in the data.

Figure 12 explores the dependence of the exponent $\lambda$ in $\sigma_{tot}^{\gamma^* p}(W^2, Q^2) \sim (W^2)^{\lambda}$ as a function of $Q^2$ from the H1 $F_2$ data.[25] There is a steady decrease in $\lambda$ with decreasing $Q^2$. The data show a smooth transition from the higher to lower $Q^2$ regions in the $Q^2$ range covered by the H1 data from 0.35 to 3.5 GeV$^2$ down to 6 x $10^{-6}$. The H1 experiment also reports[25] that the distinct rise in $F_2$ with decreasing $x$ that is observed for $Q^2 > 2$ GeV$^2$ is sharply reduced with decreasing $Q^2$ until the rise observed at small $Q^2$ is close to that expected by Regge models.
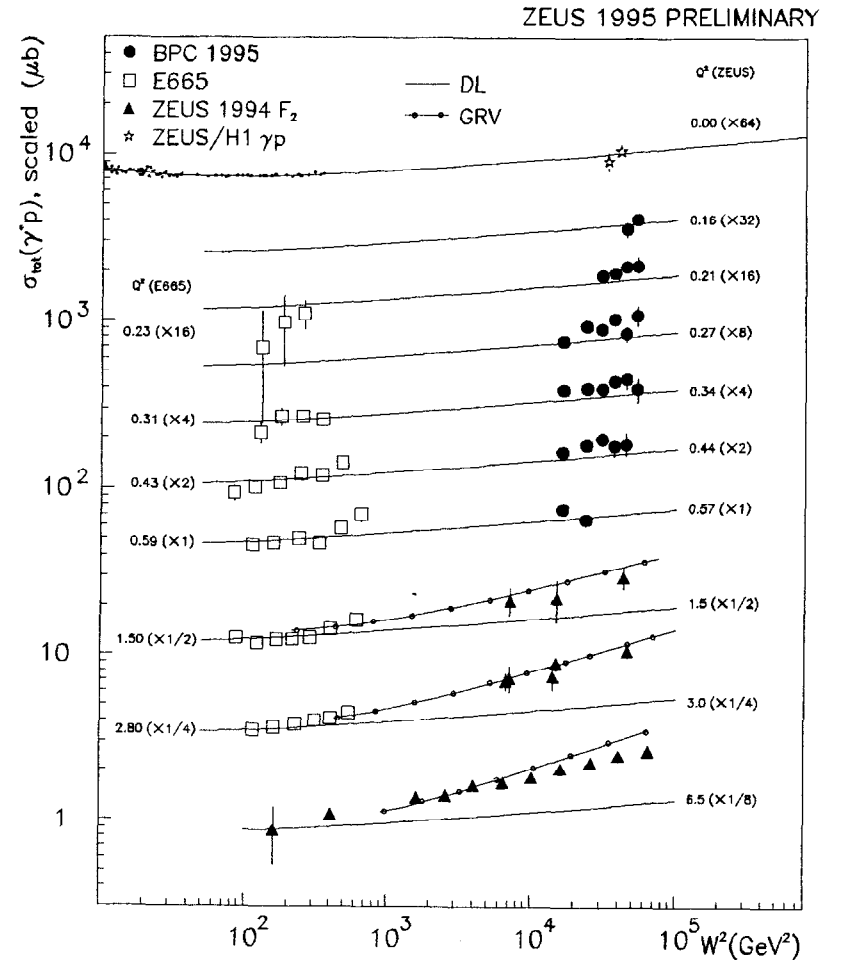


Figure 11. Total $\gamma^* p$ cross section, $\sigma_{tot}^{\gamma^* p}(W^2, Q^2) \approx \dfrac{4\pi^2 \alpha}{Q^2} F_2(x, Q^2)$ as a function of $W^2$ for ZEUS and E665. The total cross section for real photon-proton scattering from ZEUS, H1, and fixed-target experiments at low W are also shown.
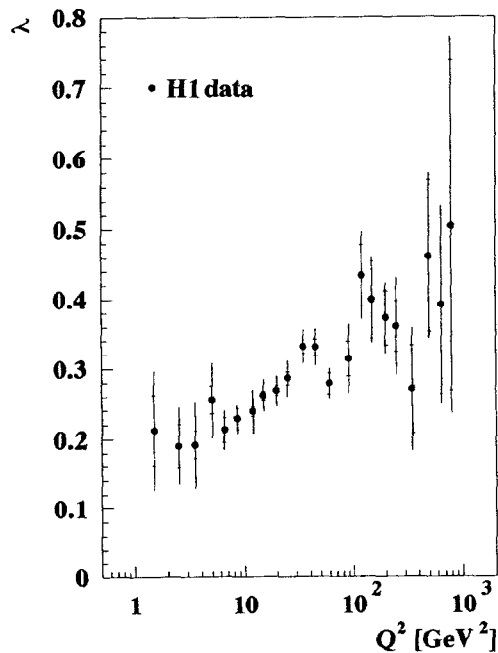
Figure 12. Dependence of $\lambda$ in $\sigma_{tot}^{\gamma^*p}(W^2,Q^2) \sim (W^2)^\lambda$ on $Q^2$ from H1.
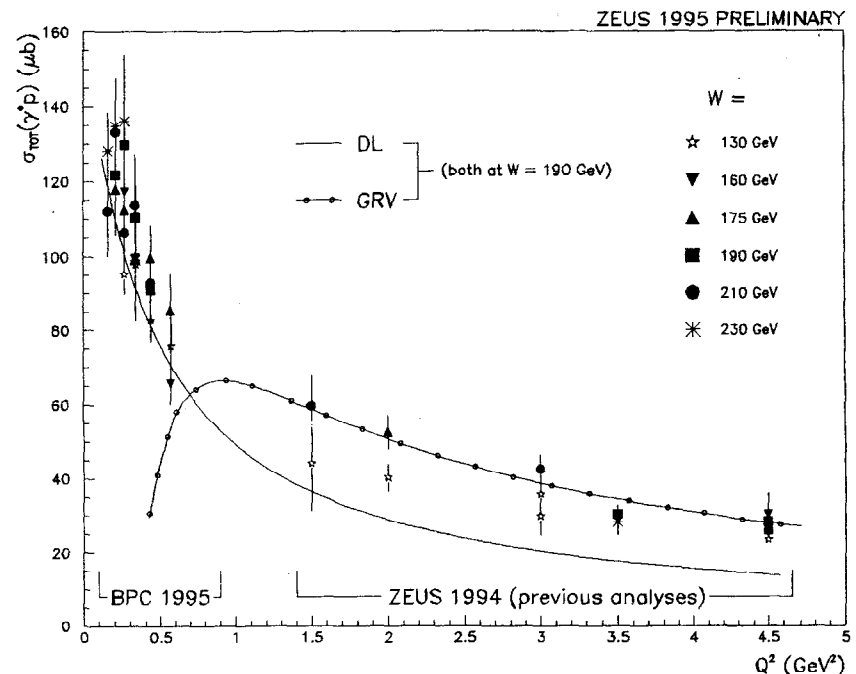


Figure 13. The total virtual photon-proton cross section $\sigma_{tot}(\gamma^*p)$ as a function of $Q^2$ from ZEUS 1995 BPC and 1994 SVX and NVX data for various mean $W^2$ values. Also shown are the predictions of GRV (upper curve for $Q^2 > 1.5$) and DL.

Figure 13 shows $\sigma(\gamma^*p)$ as a function of $Q^2$ with the cross sections at different W values indicated by different symbols. The data between $Q^2 = 0.16$ and $0.57$ GeV$^2$ show the same decrease with increasing $Q^2$ for all values of W between 130 GeV and 230 GeV. This is consistent with the Regge picture as shown by the agreement with the DL model. For $Q^2 \geq 1.5$ GeV$^2$, we again observe behavior consistent with a perturbative QCD picture as shown by the agreement with the GRV model.

Therefore, we see that the rapid rise in $F_2$ with decreasing $x$ observed by H1 and ZEUS for $Q^2 \geq 1.5$ GeV$^2$ and $x \ll 10^{-2}$ changes to a moderate rise in the low $Q^2$ region. This indicates a transition from the high-$Q^2$ perturbative QCD region to the low $Q^2$ region where Regge models provide a good description, while perturbative QCD does not. We also see that the transition region between these two regimes is smooth with an interplay between the two in the intermediate $Q^2$ range.

## 2.4. Charged and Neutral Current Cross Sections at High $Q^2$

At high $Q^2$ (> 200 GeV$^2$), the charged current and neutral current cross sections reported by H1 (Ref. 26) and ZEUS[27] have established that the $Q^2$ dependence of the CC and NC cross sections are consistent with the W and Z propagators and that the CC and NC cross sections have a similar magnitude for $Q^2 \geq M_W^2$. ZEUS has shown that the NC DIS cross section $d\sigma/dQ^2$, for $e^+p$ and $e^-p$ collisions at $200 < Q^2 < 50,000$

GeV$^2$ shows good agreement with the Standard Model and uses this to set limits of 1.0 to 2.5 TeV at 95% CL on the effective mass of contact interactions and to place a limit of $1.4 \times 10^{-16}$ cm at 95% CL on the effective quark radius. H1 have measured the integrated CC cross section and the differential cross section for $e^+p$ collisions with missing transverse momentum above 25 GeV. These results are summarized in Figure 14. Both H1 and ZEUS have used these cross sections to extract the W mass: $M_W^{H1} = 84^{+9+5}_{-6-4} GeV$, $M_W^{ZEUS} = 79^{+8+4}_{-7-4} GeV$, in good agreement with the 80.22 $\pm$ 0.26 GeV on-shell W mass measured at the Tevatron.[28]

undetected down the beampipe. We denote such events as 1+1, where the +1 refers to the unseen remnant jet. The production of additional jets in DIS beyond 1+1 involves QCD since it is due to the involvement of gluons in the hard scattering process. In particular, dijet or 2+1 jet production, to leading order in $\alpha_s$, proceeds via QCD-Compton scattering (QCDC) characterized by the emission of a gluon from the struck quark and Boson-Gluon-Fusion, where a gluon from the proton and the virtual boson fuse to form a quark-antiquark pair. The basic DIS parton emission processes up to leading order in $\alpha_s$ are shown in Figure 15. Shown are (a) the Born process where a single quark is emitted, (b) BGF, (c) QCDC where the gluon is emitted in the final state and (d) in the initial state, and (e) gluon emission in the final and initial state as viewed in the Breit Frame.[29] In the naive quark parton model, the Breit Frame is the frame where the struck quark is scattered exactly backwards to its original direction and has no transverse momentum component. However, QCD processes introduce a net transverse momentum component to the incoming parton or the struck quark itself.

The strong coupling constant, $\alpha_s$, can be measured at HERA from the relative rate of 2+1 jet events to 1+1 jet events. This measurement can be performed for different values of Q$^2$ so that it is possible to see the evolution of $\alpha_s$ within a single experiment over a wide range of Q$^2$. For the extraction of $\alpha_s$ to be reliable, the 2+1 jet rate must be calculated to NLO and the jet definition must be treated in the same way for experiment and theory.
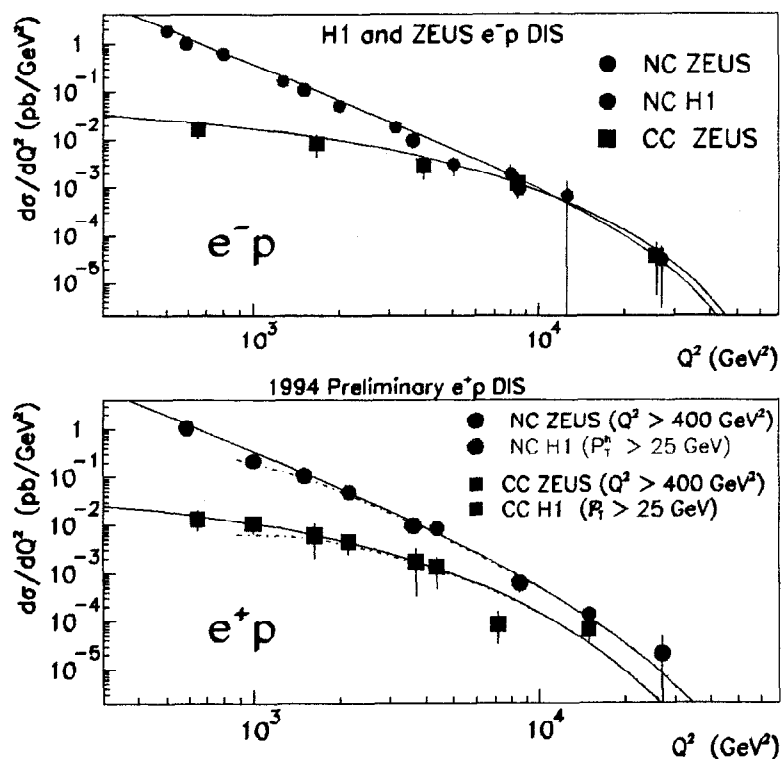
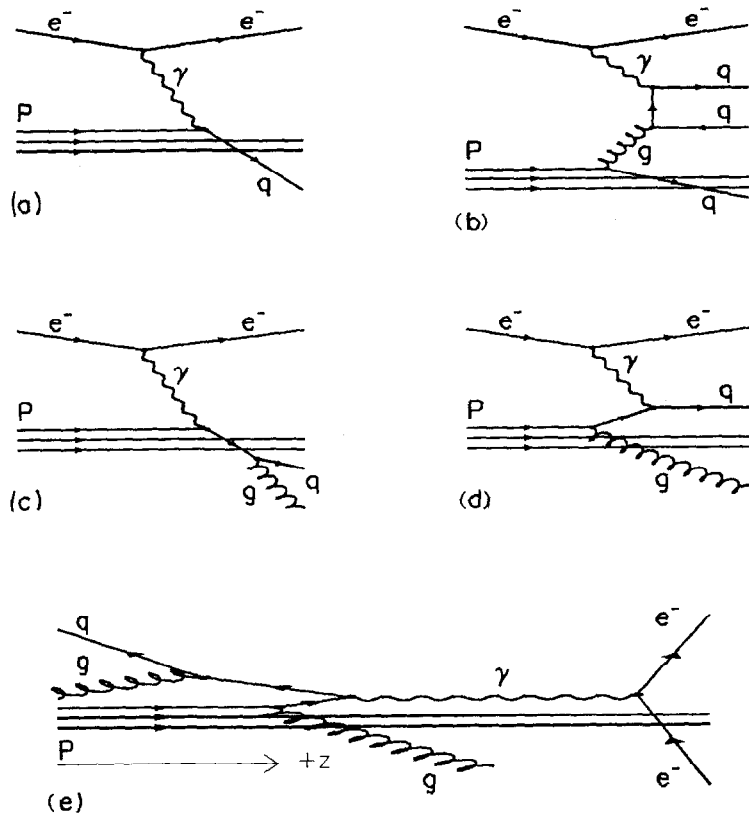Figure 14. CC and NC DIS cross sections at high Q$^2$ from H1 and ZEUS for $e^-p$ and $e^+p$ collisions, compared with Standard Model predictions.

## 2.5. Jets in Deep Inelastic Scattering

In the naive quark-parton model, DIS virtual photoproduction gives rise to one jet from the struck quark and one jet from the proton remnant, which at HERA escapes

Figure 15. DIS parton emission processes to leading order in $\alpha_s$: (a) Born process, (b) Boson Gluon Fusion, (c) final state gluon radiation, (d) initial state gluon radiation, (e) Breit Frame view of initial and final state gluon radiation.

Both H1(Ref. 30) and ZEUS[31] have extracted $\alpha_s$ from multijet production. They used the JADE[32] algorithm to assemble the jets and relate the hadronic final state measured in the detector to the hard scattering process. The algorithm employs a scaled invariant mass $y_{ij} = m_{ij}^2/W^2 = 2E_iE_j(1-cos\theta_{ij})/W^2$, where $m_{ij}$ is the invariant mass of objects $i$ and $j$, which are assumed massless and $E_i$, $E_j$ are their energies. Objects are

merged into jets by adding their four-momenta until $y_{ij}$ for all objects exceed a jet resolution parameter $y_{cut}$. To prevent the detected fraction of the proton remnant jet from forming spurious jets, a pseudo-particle[33] was inserted along the z-axis (proton direction) and the missing longitudinal momentum in each event was assigned to it. Both H1 and ZEUS extracted values of $\alpha_s$ at $y_{cut} = 0.02$. Even this value of $y_{cut}$, which requires a large invariant mass between the jets, does not constrain the jets to be away from the beam direction. This is because one of the nonremnant 2+1 jets is often in the forward direction due to the forward singularity in the cross section. This forward direction has the greatest model uncertainty. Therefore H1 impose a cut in the jet polar angle in the laboratory system ($\theta_{jet} > 10°$). They also impose a cut in the backwards direction ($\theta_{jet} < 145°$) to ensure analysis in the hadronic calorimeter. In contrast, ZEUS uses a cut on $z = 1/2(1-cos\theta^*)$, where $\theta^*$ is the angle of the parton that produced the jet in the $\gamma^*$–parton center-of-mass system, of $0.1 < z < 0.9$. The variable $z$ is a Lorentz invariant and a well-defined variable in the theory. These cuts on the jet position significantly reduce the statistics. In the case of the ZEUS cut, the loss is 50%.

Figure 16 shows the corrected jet rates $R_{1+1}$, $R_{2+1}$, and $R_{3+1}$ as a function of $y_{cut}$ for ZEUS data[31] compared with the DISJET[34] and PROJET[35] NLO QCD calculations for three $Q^2$ intervals between 120 and 3600 GeV$^2$ and the whole range. Both programs agree in their predictions for $\alpha_s$ and reproduce the shape of the measured jet rate distributions. H1 performed a similar analysis for two $Q^2$ intervals, 100–400 and 400–4000 GeV$^2$.
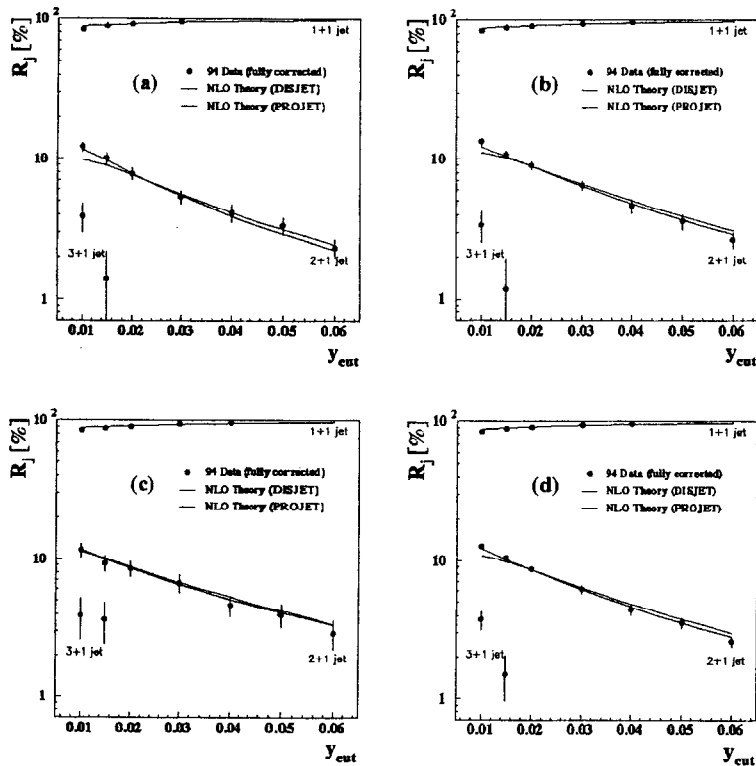
Figure 16. ZEUS results for jet production rates, $R_j$ as a function of the jet resolution parameter $y_{cut}$ for (a) $120 < Q^2 < 240$ GeV$^2$, (b) $240 < Q^2 < 720$ GeV$^2$, (c) $720 < Q^2 < 3600$ GeV$^2$, and (d) $120 < Q^2 < 3600$ GeV$^2$ with statistical errors only compared with two NLO QCD calculations, DISJET and PROJET.

The running of $\alpha_s$ depends on the renormalization group equation. The extraction of $\alpha_s$ in finite order QCD perturbative calculations depends on the renormalization scheme. H1 and ZEUS use the $\overline{MS}$ scheme. In second order, the dependence on other renormalization schemes is characterized by a single parameter, the value of the renormalization scale[36] where $\alpha_s$ is evaluated. H1 and ZEUS chose this to be $Q^2$. The same scale, $Q^2$, is chosen for the factorization scale where the parton densities are evaluated.

The ZEUS values[31] of $\alpha_s$ extracted using the JADE cluster algorithm are plotted in Figure 17 as a function of $Q^2$ for three $Q^2$ ranges. They are calculated from the fitted values of $\Lambda_{\overline{MS}}^{(5)}$ and plotted against the curves for $\Lambda_{\overline{MS}}^{(5)} = 100$, 200, and 300 MeV.

ZEUS uses five flavors in the calculation of $\Lambda$ because the lower bound of the $Q^2$ range is above the b-quark mass threshold. The measured $\alpha_s$ decreases with increasing $Q^2$ as expected from the running of the strong coupling constant if $Q^2$ is taken as the scale. Extrapolating these measurements to $Q = M_{Z^0}$ yields the ZEUS result from the JADE algorithm that $\alpha_s(M_{Z^0}) = 0.117 \pm 0.005$ (stat) $^{+0.004}_{-0.005}$ (syst$_{exp}$) $\pm 0.007$ (syst$_{theory}$). H1 also extract their result[30] using the JADE algorithm, but with four flavors in the calculation of $\Lambda$ and determine $\alpha_s(M_{Z^0}) = 0.123 \pm 0.018$, with statistics and systematic errors combined in quadrature. The difference in number of flavors should be a small effect since the contribution to the proton structure function from massive b-quarks in the kinematic region studied in these measurements is less than 2% (Ref. 37). The H1 and ZEUS values of $\alpha_s$ are in agreement with the world average result[28] of $\alpha_s(M_{Z^0}) = 0.117 \pm 0.005$. This constitutes an important test of QCD.

The ZEUS experiment also explored the dependence of the $\alpha_s$ measurement on use of another cluster algorithm, the $k_t$ algorithm, which is evaluated in the Breit frame and uses a jet resolution parameter based on the minimum transverse energy of one particle relative to the other, $y_{ij} = 2\min(E_i^2,E_j^2)(1-\cos\theta_{ij})/M_{ref}^2$, where $M_{ref}^2$ is either $Q^2$ or a fixed value of 120 GeV$^2$ (Ref. 38). A second parameter, the transverse energy of the particle relative to the incoming proton direction, $y_{ip} = 2E_i^2(1-\cos\theta_{ip})/Q^2$, is used to distinguish particles that belong to the proton remnant jet from those which form jets by the condition $y_{ip} < y_{ij}$ for inclusion in the remnant jet. The $k_t$ algorithm does not require a $z$ cut with its loss of statistics nor a pseudo-particle to take care of the remnant jet. Its detector and hadronization corrections are smaller than those of the JADE algorithm. Finally, due to the definition of the energy-angle correlation of the particles with respect to the proton direction, initial state collinear singularities can be dealt with in a well-understood manner.[29] Figure 17 shows the extracted ZEUS values[38] of $\alpha_s$ extracted using the $k_t$ cluster algorithm as a function of $Q^2$ for three $Q^2$ ranges, $M_{ref}^2$ is either equal to $Q^2$ or a fixed value of 120 GeV$^2$. Extrapolating these measurements to $Q = M_{Z^0}$ yields the ZEUS results from the $k_t$ algorithm that $\alpha_s(M_{Z^0}) = 0.118 \pm 0.008$ (stat) for $M_{ref}^2 = Q^2$ and $0.120 \pm 0.004$ (stat) for $M_{ref}^2 = 120$ GeV$^2$. These values are close to the value of 0.117 extracted using the JADE algorithm, indicating only a small dependence on the choice between the JADE and $k_t$ cluster algorithms.
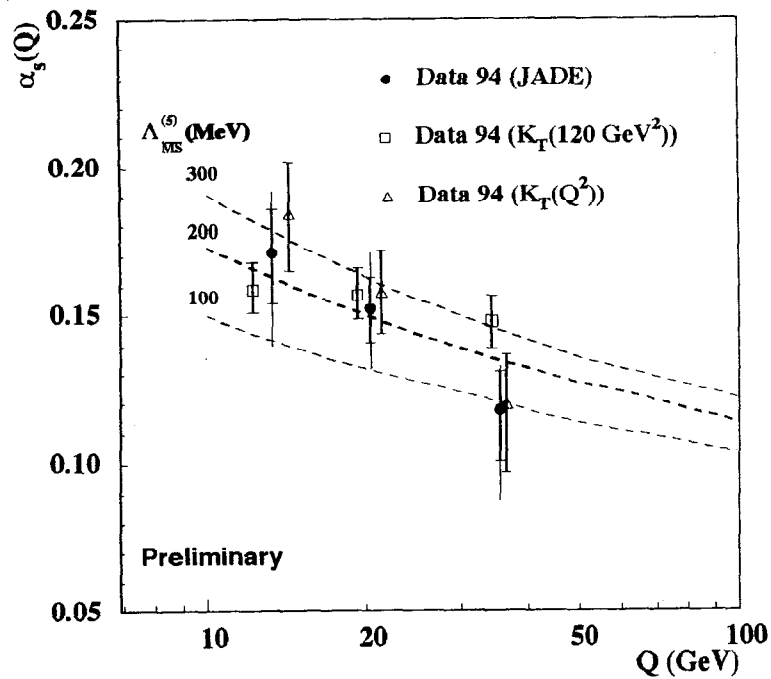
Figure 17. ZEUS measured values of $\alpha_s(Q)$ for three different $Q^2$ regions, extracted using three different jet algorithms. The statistical error corresponds to the inner bar and the thin bar shows the statistical and systematic error combined in quadrature. The dashed curves represent $\alpha_s$ with $\Lambda_{\overline{MS}}^{(5)} = 100, 200,$ and $300$ MeV.

# 3. Photoproduction

## 3.1. Introduction

For low $Q^2$ $ep$ scattering, the photon is essentially real and the involvement of the electron can be essentially neglected. Such events are therefore called photoproduction events. Since the cross section has a $1/Q^4$ dependence, these events are the most common type of $ep$ interaction. Although the center of mass of the $ep$ collisions is 300 GeV at HERA, the center-of-mass energy of the photon-proton collisions, $W_{\gamma p} = \sqrt{4yE_eE_p}$, has a range from less than 130 GeV to more than 270 GeV. This is equivalent to a beam of 20 TeV photons striking a fixed proton target. These energies are sufficiently high to permit a photon that has fluctuated into a quark-antiquark pair to travel as a hadronic particle for hundreds of proton radii without violating the Heisenberg Uncertainty Principle.
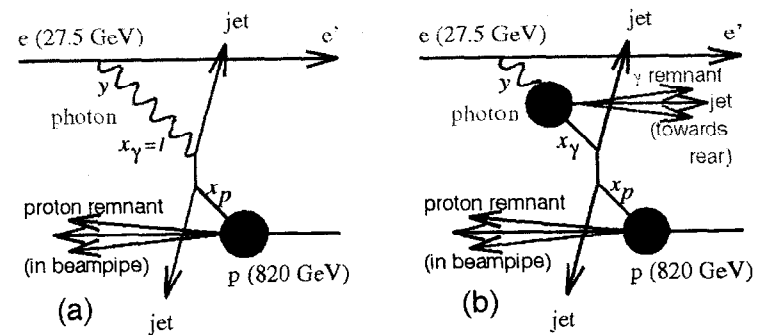


Figure 18. Topology of (a) direct photoproduction and (b) resolved photoproduction.

Photoproduction events are classified into direct and resolved[39] categories. The topology of a direct photoproduction event is shown in Figure 18(a). Direct photoproduction occurs when the photon interacts directly with a quark or gluon in the proton. In this case, the fraction of the photon momentum involved in the collision, $x_\gamma$, is close to one. Due to the low $Q^2$, the scattered electron emerges at a very low angle and travels undetected down the beampipe in the original electron direction. The hard scattering of the photon with a parton in the proton, carrying a fraction of proton momentum, $x_p$, can result in two outgoing partons with high $E_t$ that manifest themselves as two jets in the main detector. The remaining particles from the proton, which form the proton remnant jet, travel down the beampipe in the proton direction. Figure 19 shows a high-$E_t$ direct photoproduction dijet event as observed in the ZEUS detector.
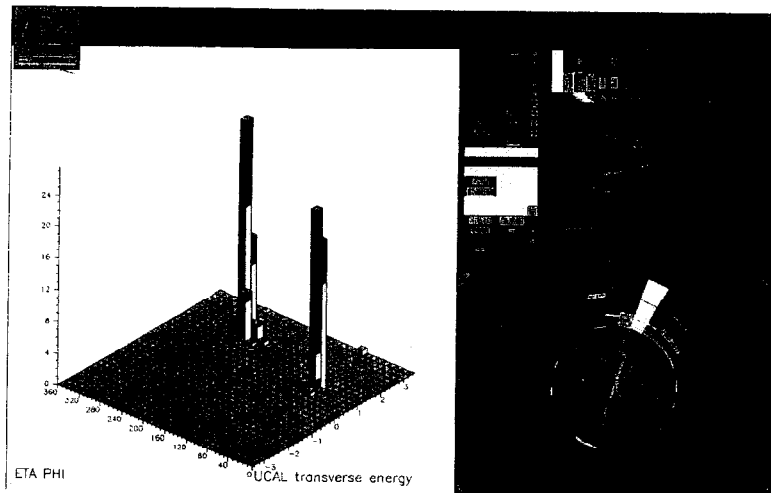


Figure 19. Direct photoproduction dijet event as seen in ZEUS.

Figure 18(b) shows the topology of a resolved photoproduction event. Here the scattered electron is also emitted at a very shallow angle. However, the high-energy photon fluctuates into a quark-antiquark pair, thereby resolving into a hadronic state before the collision. Hence, the photon acts like a source of quarks and gluons, one of which interacts with a parton from the proton. Therefore, only a fraction of the photon's momentum, $x_\gamma$, participates in the hard scatter, i.e., $x_\gamma < 1$. The remaining photon momentum is carried away by the other partons in the photon, which tend to travel close to the original photon direction, which is close to the scattered electron

direction. The fragmentation of these remaining partons from the photon is called the photon remnant and is found toward the rear of the detector. As for the case of direct photoproduction, the fragmentation of the remaining partons in the proton form the proton remnant, which travels down the beampipe in the proton direction. Figure 20 shows a resolved photoproduction event from ZEUS with two high-$E_t$ dijets and a photon remnant observable in the rear of the detector.
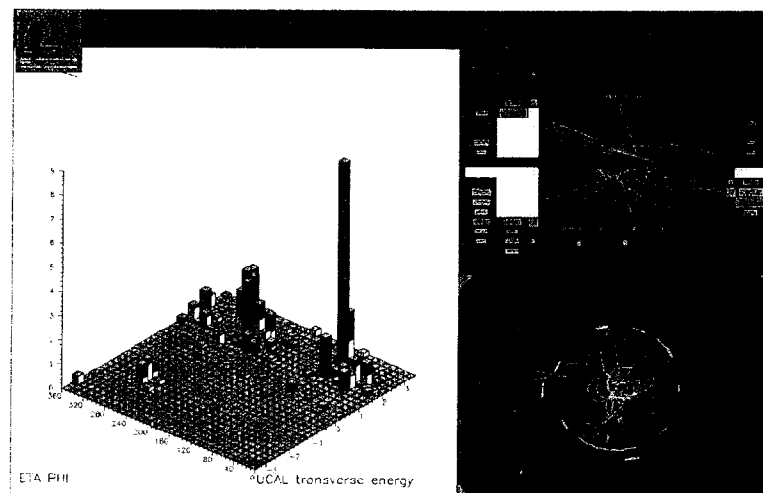


Figure 20. Resolved photoproduction high-$E_t$ dijet event as seen in ZEUS. Note the presence of the photon remnant in the rear of the detector.

## 3.2. Models of Photoproduction

In Leading Order (LO) QCD, for direct photoproduction [Figure 21(a)], the photon interacts via boson-gluon fusion or QCD Compton scattering. These processes have a quark propagator in the $s$, $t$, or $u$ channel, with the $t$ and $u$ channels dominating. For resolved photoproduction [Figure 21(b)], the dominant subprocesses (e.g., $qg \rightarrow qg$, $gg \rightarrow gg$, $qq \rightarrow gg$) involve the $t$-channel exchange of a gluon. Since the $Q^2$ of the photon is generally below 1 GeV, perturbative QCD cannot be used to describe the fluctuation of the photon into a hadronic state. Therefore, the photon is treated as a strongly interacting particle and a parton distribution function (PDF) is used to describe its structure. This model is called vector-meson dominance (VMD)[40] since the photon must fluctuate into a meson with the same spin 1. Photon-PDF's are used to parameterize the probability to find a parton in the photon that carries a fraction of the

photon's momentum, $x_\gamma$. The circles in the diagrams in Figure 21 indicate the PDF's for the photon and proton.



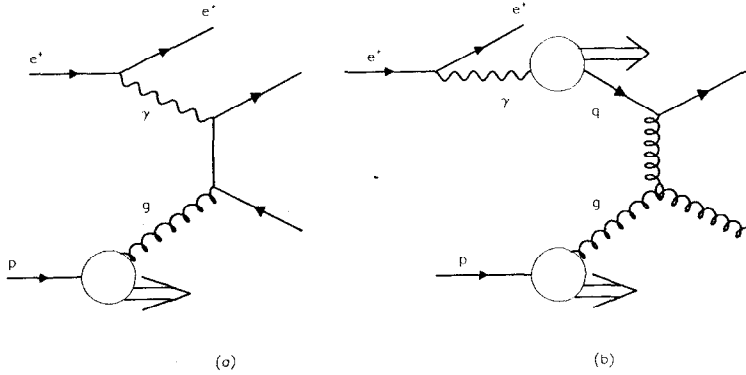(a)                                        (b)

Figure 21. Examples of LO QCD diagrams for (a) direct photoproduction and (b) resolved photoproduction.

At Next-to-Leading-Order (NLO) in QCD, the distinction between direct and resolved photoproduction blurs. Therefore, a separation of resolved and direct photoproduction was developed,[41] based on the variable

$$x_\gamma^{OBS} = \frac{\sum_{jets} E_T^{jet} e^{-\eta^{jet}}}{2yE_e},$$

where the sum runs over the two highest $E_T$ jets, $\eta_{jet} = -\ln(\tan\theta/2)$ is the pseudorapidity of the jet, where $\theta$ is the angle of the jet axis, and $y = E_\gamma/E_e$ is the fraction of the initial electron energy carried by the photon. $x_\gamma^{OBS}$ is the fraction of the photon's energy participating in the production of the two highest $E_T$ jets. This variable is calculable to all orders in perturbative QCD and is measurable. However, an additional complication to the measurement of the jet energy is the contribution to the underlying event energy from the spectator partons that produce the proton remnant jet. Such multiparton interactions in beam remnants[42] have been used to describe hadron collider data.[43] Since the dynamics of hadronic final state interactions in hadronic collisions should resemble those found in high-energy photoproduction in $ep$ collisions, these models have been applied to HERA data.[44,45]

## 3.3. Jets in Photoproduction

Figure 22 shows the $x_\gamma^{OBS}$ distribution for ZEUS data[46] using the $k_T$ jet clustering algorithm described in Sec. 2.5. The peak at high $x_\gamma^{OBS}$ is from direct photoproduction, while resolved photoproduction extends the tail down to low $x_\gamma^{OBS}$, where the forward rapidity acceptance for jets cuts off. Events from the HERWIG 5.8 Monte Carlo[47] are shown with and without multiparton interactions.[45,48] The Monte Carlo is normalized to agree with the data for $x_\gamma^{OBS} > 0.3$. Irrespective of the multiparton interactions, both Monte Carlo histograms do not match the data for $x_\gamma^{OBS} < 0.3$, although the inclusion of multiparton interactions moves the histogram closer. For $x_\gamma^{OBS} > 0.3$, the HERWIG Monte Carlo with multiparton interactions provides a good description of the data. Therefore, ZEUS measures resolved photoproduction for $x_\gamma^{OBS} > 0.3$. Also shown as the dark histogram is the HERWIG LO direct contribution, with a vertical line drawn at $x_\gamma^{OBS} = 0.75$ to define the region above this cut that corresponds to the LO definition of direct photoproduction. Therefore, for data and calculations, we define resolved and direct photoproduction by this cut in $x_\gamma^{OBS}$.
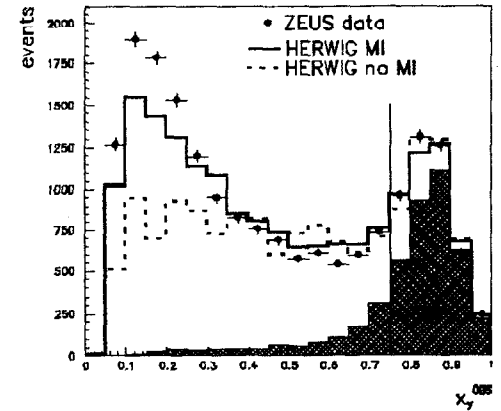


Figure 22. $x_\gamma^{OBS}$ of ZEUS data without acceptance correction (black dots) compared to HERWIG Monte Carlo with and without multiparton interactions including all acceptance effects. The shaded histogram is the subset of LO direct HERWIG events.

### 3.3.1. Inclusive Jet Cross Sections

The photoproduction jet cross section as a function of transverse energy, $d\sigma/dE_T^{jet}$, falls steeply with $E_T$, as predicted by QCD. The measured cross section is described by matrix elements summed according to the quark and gluon distributions of the quark and gluon distributions in the proton and photon, and is relatively less sensitive to these distributions than to the features of the matrix elements. The photoproduction jet cross section as a function of the pseudo-rapidity, $d\sigma/d\eta^{jet}$, is sensitive to the parton distributions in the photon and can be used to extract them.

Figure 23 shows the inclusive differential jet photoproduction cross sections, $d\sigma/dE_T^{jet}$ and $d\sigma/d\eta^{jet}$, from H1 (Ref. 49). The H1 data is plotted using the pseudo-rapidity in the lab frame, where $\eta(lab) - \eta(cms) = 0.5 \ln(E_p/E_\gamma) \approx 2$. Figure 23(a) shows the $E_T$ spectrum measured in two jet pseudo-rapidity intervals, $-1 < \eta_{jet} < 1$ and $-1 < \eta_{jet} < 2$. Figure 23(b) shows the jet cross section as a function of $\eta_{jet}$ for three different jet $E_T$ thresholds: $E_t^{jet} > 7$, 11, and 15 GeV. The cross section decreases as $(E_T^{jet})^{-n}$ with $n = 6.1 \pm 0.5$ between $7 < E_t^{jet} < 29$ GeV, and $-1 < \eta_{jet} < 2$. The ZEUS experiment also reports similar results[50] and has extended these measurements to higher $E_T$ and compared them with NLO QCD calculations.[51] The H1 and ZEUS results are consistent with the jet cross sections measured in hadron collisions at the same cms energy of 200 GeV (Ref. 52), where an exponent of $n = 5.8$ was measured for the same $E_t^{jet}$ range.

Figure 23 compares the H1 data with a calculation based on the PYTHIA 5.7 event generator for photon-proton interactions.[53] The PYTHIA model without multiple interactions (dashed line) does not describe the measured cross sections well at large
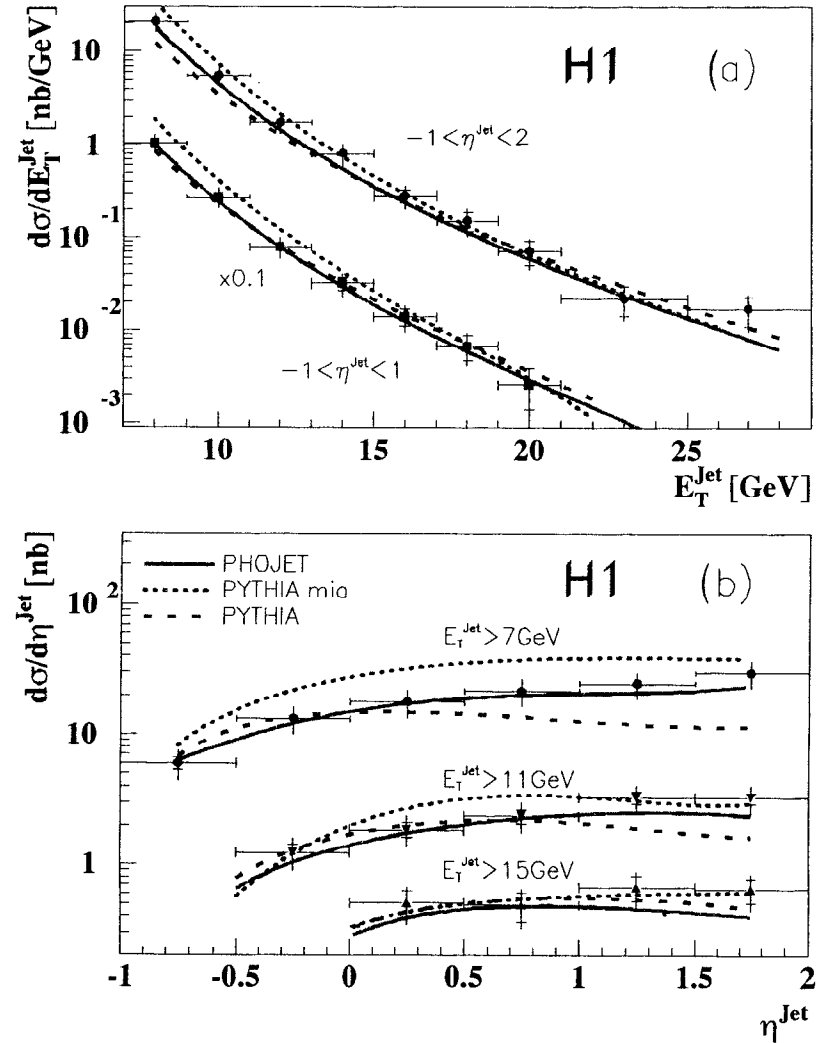


Figure 23.(a) Inclusive differential $E_T^{jet}$ photoproduction jet cross sections for $E_T^{jet} > 7$ GeV from H1 for two $\eta$ ranges compared with two QCD generators, PHOJET and PYTHIA, the latter with and without interactions of the beam remnants.(b) Inclusive differential $\eta$ photoproduction cross section from H1 compared with the same 3 QCD generators for 3 different $E_T^{jet}$ thresholds.[49]

rapidities and at small transverse energies of the jets. The PYTHIA model with multiple interactions (dotted line) provides a good description of the shape of the measured $d\sigma/d\eta^{jet}$ cross section, but gives too large a cross section for small $E_t^{jet} > 7$ GeV, where $x_\gamma$ is small ($x_\gamma \approx 0.1$). Figure 23 also compares the H1 data with the PHOJET 1.0 calculation,[54] which includes multiple interactions, but with softer beam-remnant interactions than PYTHIA, and adds a characterization of the transition to the nonperturbative soft-scattering. In addition, while PYTHIA contains hard initial state parton radiation, PHOJET does not. The PHOJET curves (solid lines) give a good description of both $d\sigma/dE_T^{jet}$ and $d\sigma/d\eta^{jet}$ distributions. The differences in these two models and their agreement with the data lead H1 to conclude that there are uncertainties on the order of a factor of two in conclusions about the parton content of the photon drawn from jet cross sections in the low $x_\gamma$ region.[49] The data support the inclusion of interactions between the beam remnants since this produces a marked improvement in the agreement with QCD models.

### 3.3.2. Dijet Photoproduction Cross Sections

Figure 24 shows the kinematics of dijet production in the dijet center-of-mass system and the lab frame. In the dijet CMS, the average pseudo-rapidity of the two highest $E_T$ jets, $\bar{\eta} = \frac{1}{2}(\eta_1 + \eta_2) = \frac{1}{2}\ln\frac{x_p E_p}{yx_\gamma E_e}$, provides information about the structure functions of the photon and proton. The sensitivity to the incoming particle parton distributions is increased by the requirement[55] that $|\Delta\eta| = |\eta_1 - \eta_2| < 0.5$. Under these conditions

where $E_T^{jet1} \approx E_t^{jet2}$, for $2 \rightarrow 2$ scattering in LO QCD, we have: $x_\gamma \approx \frac{\left(E_T^{jet}e^{-\eta^{jet}}\right)}{yE_e} \propto \frac{\bar{\eta}}{y}$

for resolved photoproduction ($0.3 < x_\gamma^{OBS} < 0.75$, where the lower cut is placed to ensure a well-understood model) and $x_p \approx \frac{\left(E_T^{jet}e^{+\eta^{jet}}\right)}{E_P} \propto \bar{\eta}$ for direct photoproduction ($x_\gamma^{OBS} > 0.75$). This provides an opportunity, by separating direct from resolved photoproduction, to present cross sections sensitive to the gluon distributions in the proton and photon, respectively.
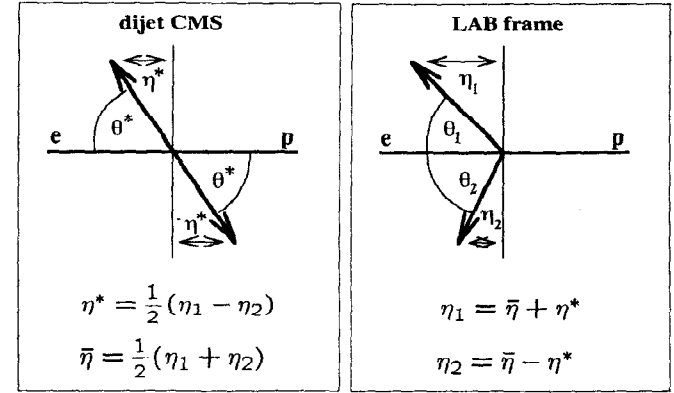


Figure 24. Jet kinematics for *ep* interactions in the center-of-mass system and the lab frame.

Figure 25 shows the differential dijet cross section, $d\sigma/d\bar{\eta}$, from ZEUS[56] integrated above $E_T^{jet} = 6$ GeV for the central rapidity range, $-1.375 < \eta_{jet} < 1.875$ using three different jet finders. EUCELL and PUCELL are cone algorithms[57] with radius R =1. EUCELL uses a sliding window in $\eta$ and $\phi$ to define the seed, while PUCELL uses a calorimeter cell as a seed and merges nearby jets under certain conditions. KTCLUS[58] is a $k_T$ cluster algorithm (see Sec. 2.5) selected[59] to closely resemble the cone algorithm in its use of $\Delta R = \sqrt{(\Delta\phi)^2 + (\Delta\eta)^2}$ and the $E_T$ recombination scheme. Also shown is a full NLO QCD calculation of Klasen and Kramer[56] using the GRV[60] photon and CTEQ[61] proton PDF's for $R_{sep} = 1.0$ and 2.0, where $R_{sep}$ (Ref. 62) determines the maximum distance in $\eta-\phi$ at which two partons can be merged into a single jet. For comparison with KTCLUS and PUCELL, $R_{sep} = 1.0$ should be used, and for comparison with EUCELL, $R_{sep}$ should be in the range 1.5–2.0. In Figure 25(a), the direct photoproduction data is in fairly good agreement with the theory, particularly when the KTCLUS algorithm is used, with the exception of the forward rapidity region, where the data fall systematically above the theory. The choice of jet algorithm has an effect of about 25–30% for both theory and experiment. In Figure 25(b), the resolved cross section data is above the theory by a factor of two, although the systematic errors are large and the shape appears to be generally the same. The choice of jet algorithm has an effect of about 50% in both theory and experiment.
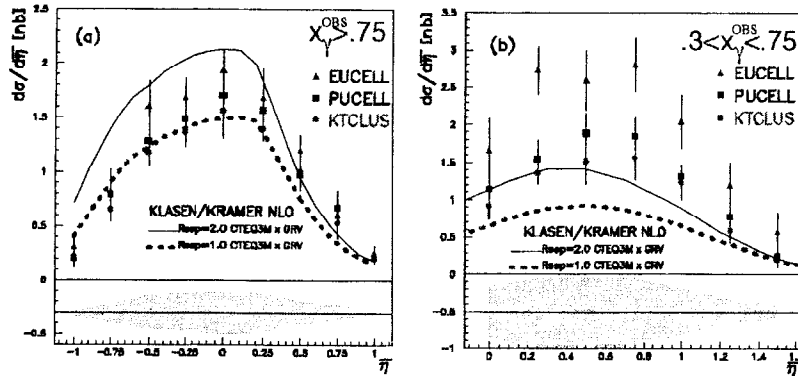
Figure 25. Differential dijet cross section, $d\sigma/d\bar{\eta}$ , for three different jet algorithms from ZEUS for (a) direct photoproduction and (b) resolved photoproduction. The shaded band indicates the uncertainty due to the ±5% uncertainty in the calorimeter energy scale. The curves are from the full QCD NLO calculations described in the text.

### 3.3.3. Dijet Angular Distributions in Photoproduction

The difference between the pseudo-rapidity of the two highest $E_T$ jets, $\eta^*$, where $\tanh(\eta^*) = \tanh(1/2(\eta_1 - \eta_2)) = \cos(\theta^*)$ and $\theta^*$ is the angle between the jet-jet axis and the beam direction in the dijet CMS (see Figure 24), provides information about the spin of the exchanged particle in the interaction. Only the absolute value of $\cos\theta^*$ can be measured since the outgoing jets are indistinguishable. As shown in Figure 21 and discussed in Sec. 3.2, LO QCD direct photoproduction involves a quark propagator, while resolved photoproduction processes are dominated by a gluon propagator. The angular dependence of the cross section for resolved processes with a spin-1 gluon propagator is approximately proportional to $(1-|\cos\theta^*|)^{-2}$, whereas the angular dependence of direct photoproduction with a spin-1/2 quark propagator is approximately proportional to $(1-|\cos\theta^*|)^{-1}$. Therefore, the cross section for resolved processes should rise more steeply with increasing $|\cos\theta^*|$ than direct processes. This behavior is also predicted by NLO QCD calculations[63].

In order to enhance the sensitivity to the parton dynamics, ZEUS makes a cut[64] on $\bar{\eta}$, which is a measure of the boost of the dijet scattering system in the HERA frame, $|\bar{\eta}| < 0.5$. This is in contrast to the requirement of $|\Delta\eta| = |\eta_1 - \eta_2| < 0.5$ used to enhance the sensitivity of the dijet cross sections to the incoming parton distributions. In addition, the dijet angular distributions are studied with a cut on the dijet invariant mass, $M_{jj} > 23$ GeV, where $M_{jj} = \sqrt{2 E_T^{jet1} E_T^{jet2} \left[\cosh\left(\eta^{jet1} - \eta^{jet2}\right) - \cos\left(\phi^{jet1} - \phi^{jet2}\right)\right]}$,

and $\phi^{jet}$ is the azimuthal angle of the jet in the HERA frame. For two jets back to back in $\phi$ and with equal $E_T^{jet}$, $M_{jj} \approx 2 E_T^{jet}/\sqrt{1-|\cos\theta *|^2}$ . In a LO 2 $\rightarrow$ 2 scatter, the dijet invariant mass is related to $x_p$ and $x_\gamma$ by $M_{jj} = \sqrt{4 E_\gamma E_p x_\gamma x_p} = \sqrt{4 E_e E_p y x_\gamma x_p}$ . Therefore, the requirements that the dijet system have high mass and small boost select events with $\gamma p$ center-of-mass energies mostly above 190 GeV and suppress events with low $x_\gamma^{OBS}$. This produces dijets with good acceptance over a wide range of scattering angles in a region of $x_p$ and $x_\gamma$ where photon and parton distributions are fairly well determined[64].

Figure 26(a) shows the ZEUS data[64] compared to LO and NLO QCD parton level calculations[63] using CTEQ3M[65] and GRV (LO)[60] PDF's for the proton and photon respectively. The resolved cross section rises more steeply with increasing $|\cos\theta *|$ than the direct cross section. The good agreement between data and theory verifies the expected effects of the spins of the quark and gluon propagators. The same conclusion is drawn from Figure 26(b), where the ZEUS data is compared with HERWIG58 (Ref. 47) and PYTHIA57 (Ref. 42) predictions using the MRSA[66] and GRV (LO)[60] PDF's for the proton and photon respectively. The agreement of $|\cos\theta *|$ dependence of the measured cross section with these QCD NLO calculations and Monte Carlo simulations, including parton showering and hadronization models, provides an important confirmation of fundamental aspects of QCD.
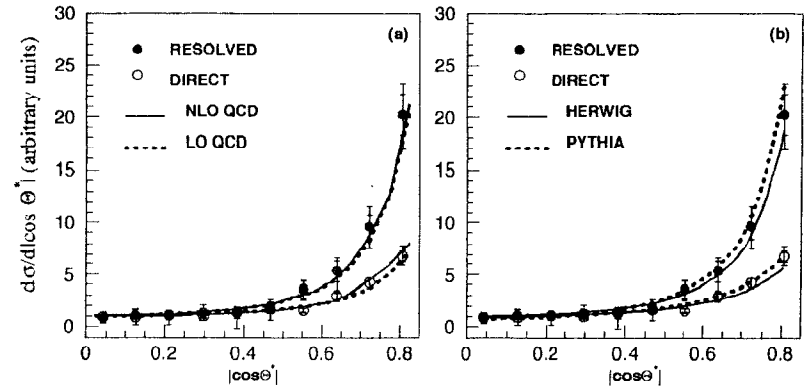


Figure 26. $d\sigma/d|\cos\theta *|$ from ZEUS[64] normalized to one at $\cos\theta^* = 0$ for resolved (black dots) and direct (open circles) photoproduction. In (a), the data are compared to a LO (dashed line) and NLO (solid line) QCD prediction. In (b), the data are compared to PYTHIA (dashed line) and HERWIG (solid line) distributions. The inner error bars show the statistical errors and the outer error bars sum in quadrature the statistical and systematic errors excluding the energy scale and luminosity uncertainties.

# 4. Diffraction

## 4.1. Soft Diffractive Phenomenology

Soft diffractive *ep* physics involves the study of soft hadronic collisions. These processes have a scale of about 1 fm. An example is *pp* scattering. The total cross section is approximately constant above 5 GeV. The elastic cross section is a large fraction at low energy (below 1 GeV) and a small fraction at high energy (above 10 GeV). If one models this cross section as a totally absorbing disk, one concludes that the elastic cross section equals the inelastic cross section and corresponds to the optical diffractive or shadow scattering observed when a plane wave impinges on a totally absorbing target, where the angular distribution is the Fourier transform of the target.[67] In the case of the hadronic cross section, as for the optical case, minima occur at angular deflections corresponding to specific values of $q^2$. While the experimental hadronic elastic cross sections display this behavior, their magnitude and dependence on energy do not.

### 4.1.1. Regge Theory

The optical theorem relates the imaginary part of the forward scattering amplitude to the total cross section, Im $F(s,t=0) = (q/4\pi) \sigma_{tot}(s)$. Using the optical theorem with unitarity and analyticity properties of the scattering amplitude leads to the Froissart bound[68] on the scattering amplitude, $\sigma_{tot}(s) < c \, (\ln[s])^2$ as $s \rightarrow \infty$. A useful description of pion-nucleon scattering above the resonance region ($M_{\pi p} > 3$ GeV), where the energy dependence is smooth, is in terms of a *t*-channel exchange two-body scattering process mediated by a single virtual particle (e.g., a pion). However, such a scattering amplitude has dominant poles corresponding to the exchange of particles with a fixed angular momentum, *j*, producing a dependence $E^j$ in the amplitude that violates the Froissart bound as $s \rightarrow \infty$.

Regge[69] showed that the usual partial wave decomposition of the scattering amplitude, $f(k,\theta) = \sum_l (2l+1) f_l(k) P_l(\cos\theta)$, could be extended to continuous complex angular momenta $f(j,k)$ with physically observable states for multiples of integral or half-integral angular momentum, $j(k)$, called Regge poles. Chew and Frautschi[70]

extended this to relativistic field theory where the resonances at these values of angular momentum, $j(t)$, are organized in a family of particles, with different spin but the same internal quantum numbers, called Regge trajectories. These turn out to have a universal slope for both baryons and mesons of the form $j(t) = j(0) + \alpha' t$, where $\alpha' \approx 1$ GeV$^{-2}$. Crossing symmetry and with the assumption that an isolated Regge pole at lowest *j* for space-like *t* dominates the amplitude results in a prediction[71] for the asymptotic behavior of the scattering amplitude in the *s*-channel, $F(s,t) \propto \dfrac{1}{k} \beta(t) \left( \dfrac{s}{s_0} \right)^{\alpha(t)}$ and

$d\sigma/dt = \beta^2(t) s^{2(\alpha(t)-1)}$. The forward direction is $t = 0$, and as we move away from the forward direction, *t* becomes negative and $d\sigma/dt$ decreases exponentially. This forward diffraction peak is an important feature of elastic scattering. Regge theory predicts that this diffraction peak should become increasingly narrower at higher *s*. This is called shrinkage.

A nearly constant total cross section at high *s* requires $\alpha(0)$ very close to one. Since a single Regge trajectory should account for all elastic scattering at high energy, where no quantum numbers save angular momentum may be exchanged, the trajectory must involve the exchange of no quantum numbers except angular momentum and therefore has the quantum numbers of the vacuum. This trajectory is called the Pomeron trajectory, where $\alpha(t) = \alpha_0 + \alpha' t = 1.085 + 0.25t$. Regge theory provides a good description[72] of total hadronic and photoproduction cross sections[73].

## 4.2. Hard Diffraction at Hadron Colliders

In 1984, the UA4 experiment at the CERN SPS $p\bar{p}$ collider reported[74] diffractive production of high mass systems at $\sqrt{s} = 540$ GeV. Ingelman and Schlein[75] suggested that high-$p_t$ jets might be produced in such states and that such high-$p_t$ structure would provide new information about the nature of Pomeron exchange. They suggested the possibility of probing the exchanged Pomeron in a hard scattering process such as between a gluon in the Pomeron and a parton in the proton, which would have the signature of two high-$p_t$ jets and two low-$p_t$ remnant or spectator jets. They also pointed out that if there were a Pomeron component in the proton that could be characterized by an effective structure function, this could be studied at HERA, where the probe would be well understood and with a clear experimental signature: "a quasi-elastically scattered proton (going down the beampipe) well separated from the hadronic system."

Subsequently, the UA8 experiment at the CERN SPS $p\bar{p}$ collider reported jet production in high-mass diffractive final states[76] that was in good agreement with a hard scattering model with a Pomeron dominated by gluons. They also reported[77] a "super-hard" component of the Pomeron, where it appeared that a "large fraction of the Pomeron's momentum participates in the hard scattering a significant amount of the time." There have also been recent measurements of diffractive scattering at the Fermilab Tevatron $p\bar{p}$ collider. These are discussed in the article by M. Albrow in these proceedings.

## 4.3. DIS Diffraction at HERA

In 1993, ZEUS reported[78] and H1 confirmed[79] DIS events that have an absence of energy deposition in the forward direction. Figure 27 shows an event observed in the ZEUS detector with no significant deposit of energy beyond $\theta > 90°$. The figure also shows the lines of pseudorapidity, $\eta$, at the boundary of the ZEUS forward, barrel, and rear calorimeters. Events with a large region in $\eta$ with no energy deposits are called large rapidity gap events (LRG). In order to quantify the absence of energy in the detector, the ZEUS analysis defines a calorimeter cluster as an isolated set of adjacent cells with summed energy above 400 MeV. The $\eta$ of the cluster closest to the forward direction, i.e., the highest $\eta$ value, is called $\eta_{max}$. Figure 28 shows the $\eta_{max}$ distribution of DIS events from ZEUS. There are two groups of events, one with large $\eta_{max}$ values, and the other with $\eta_{max} < 2$. Also shown is the standard ZEUS DIS MC, which agrees with the data for $\eta_{max} > 2$, but not for $\eta_{max} < 2$, where there is a clear excess of events with large rapidity gaps, corresponding to ~ 10% of the total DIS cross section.

A natural interpretation of these events is that they are due to diffractive scattering of the virtual photon from the proton. This means that the proton does not fragment into a visible system of hadrons either because it remains intact or dissociates into a system which is closely confined to the proton direction. In addition, there is no appreciable amount of initial state QCD radiation, because that would also have produced hadrons visible in the forward calorimeter.
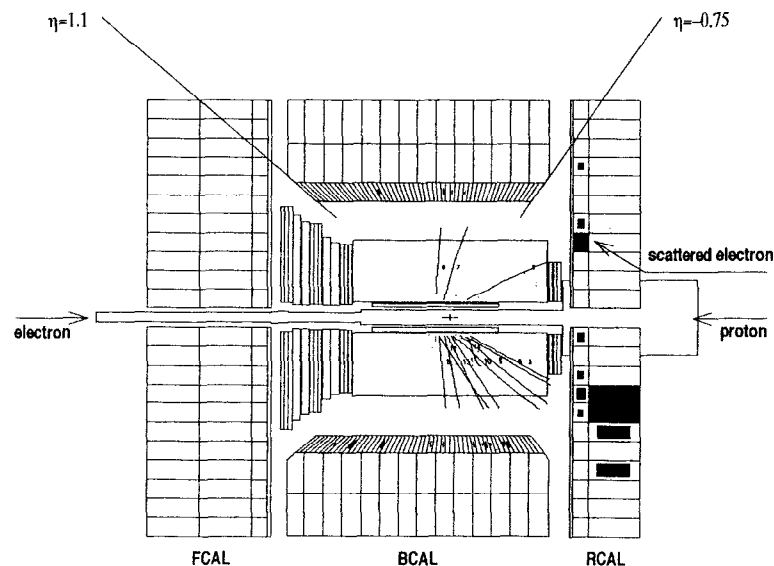


Figure 27. A ZEUS DIS event at $Q^2$=64 GeV$^2$ with a large rapidity gap.

Figure 29 shows a schematic picture of DIS events with no rapidity gap (NRG) and with a large rapidity gap (LRG). A typical NRG event has the phase space between the current jet and the proton remnant filled with particles produced by the emission of additional gluons and quarks created by the color flow between the struck quark and the proton remnant. An explanation for the LRG events is the emission of a color-neutral particle from the proton, which interacts with the exchanged virtual photon. In this case, there is no color flow that would produce particles between the struck quark and the proton remnant. Since diffraction is considered to proceed by the exchange of a Pomeron, with the quantum numbers of the vacuum, a model of the LRG events is to assume a flux of Pomerons in the proton. Figure 28 shows the prediction of a DIS model with a diffractive component (POMPYT[80]) modeled by a flux of Pomerons (where the Pomeron is considered to be composed of gluon constituents typically carrying a large fraction of the Pomeron's momentum), which does agree for all values of $\eta_{max}$.
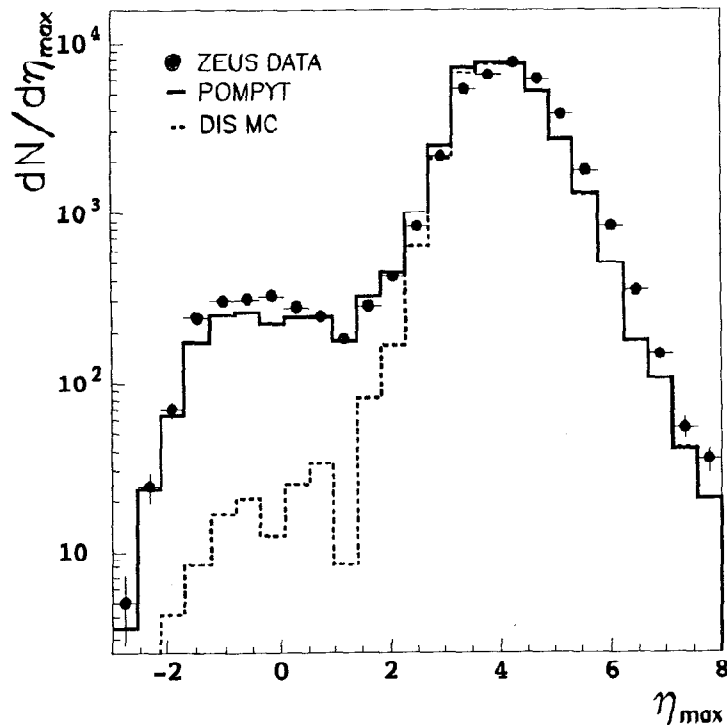
Figure 28. Distribution of the maximum rapidity $\eta_{max}$ of a calorimeter cluster in ZEUS DIS events for data (points), the standard DIS MC, and MC calculations (POMPYT) adding a diffractive component to the standard DIS processes.
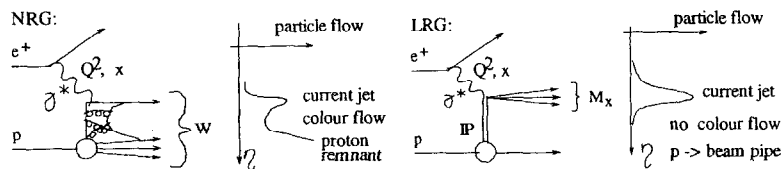


Figure 29. Comparison of *ep* events with no rapidity gap (NRG) and with a large rapidity gap (LRG), showing the absence of the particle and color flow in LRG events.

## 4.4. Analysis of Diffractive *ep* Scattering

### 4.4.1. Introduction

Diffractive *ep* scattering provides the opportunity to explore the interplay of soft and hard QCD processes as well as to investigate the structure of the Pomeron. Soft hadronic processes occur on the scale of ~ 1 fm and are characterized by the Pomeron trajectory as described in Sec. 4.1. Hard QCD processes such as DIS, including hard diffraction, have their hard scale determined by the virtuality of the photon or jets and the soft scale set by the size of the proton of ~ 1 fm. In order to apply perturbative QCD to hard processes, the hard scale physics must factorize from the soft scale physics. This factorization, which allows the two scales of physics to be considered separately, is an assumption used to produce the DGLAP evolution equations described in Sec. 2.2.3.

Important distinguishing features of hard and soft QCD processes are the energy and $t$-dependence of the scattering cross sections and their variation with $Q^2$ or $W^2$. Another interesting question is the partonic structure of the Pomeron. This can be investigated by comparison with various models treating the parton as composed of combinations of soft and hard quarks and gluons. Another approach is to treat the Pomeron as a quasi-hadron with a flux factor and under diffractive conditions to replace the proton structure function by a diffractive structure function. Another indication of Pomeron partonic structure would be jet production in diffractive events. Each of these aspects is discussed below.

### 4.4.2. Kinematics of Diffractive *ep* Scattering

Figure 30 shows the definition of the kinematic variables used in *ep* scattering. The square of the momentum transfer at the proton vertex is $t = (p - p')^2$, where $p'$ is the four-momentum of the outgoing proton, or if the proton dissociates, the four-momentum of the outgoing system. The Pomeron carries momentum $IP$, with a fraction of the proton momentum $x_{IP}$. $M_X$ is the invariant mass of the hadronic system produced from the photon dissociation. $\beta$ is the fraction of the Pomeron momentum carried by the parton in the Pomeron that interacts with the virtual photon, in analogy to the definition of $x$ defined for the proton in DIS.
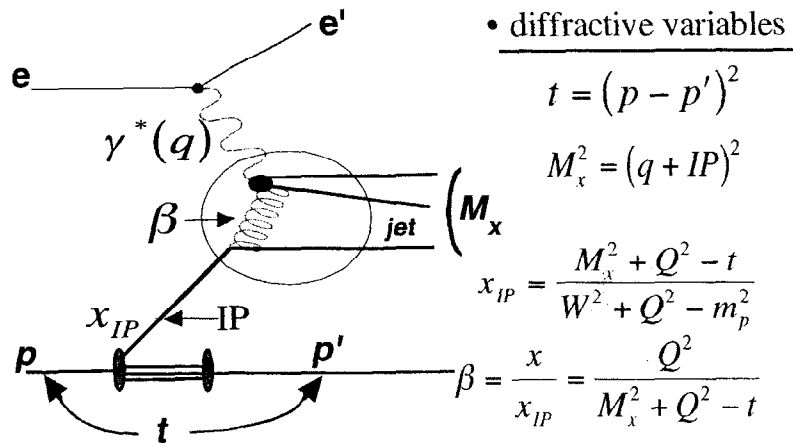
Figure 30. Definition of kinematics for diffractive *ep* scattering.

• diffractive variables

$$t = (p - p')^2$$

$$M_x^2 = (q + IP)^2$$

$$x_{IP} = \frac{M_x^2 + Q^2 - t}{W^2 + Q^2 - m_p^2}$$

$$\beta = \frac{x}{x_{IP}} = \frac{Q^2}{M_x^2 + Q^2 - t}$$

## 4.5. Diffractive Structure Function

For unpolarized beams, the differential cross section for single diffractive dissociation can be described[81] in terms of a diffractive structure function, $\frac{d^3\sigma_{diff}}{d\beta dQ^2 dx_{IP}} = \frac{2\pi\alpha^2}{\beta Q^4}(1 + (1-y)^2)F_2^{D(3)}(\beta, Q^2, x_{IP})$, where an integration has been performed over $t$, corresponding to the (undetected) momentum transfer to the proton system, the effect of $F_L$ has been neglected, and the relation $x = \beta x_{IP}$ has been used. In the model of Ingelman and Schlein,[75] the proton emits a Pomeron which is treated as a virtual hadron whose structure is probed by the virtual photon. The Pomeron is described by a structure function, $F_2^{IP}(\beta, Q^2)$, which is independent of the process of Pomeron emission Therefore $F_2^{D(3)}$ factorizes as: $F_2^{D(3)}(\beta, Q^2, x_{IP}) = f_{IP}(x_{IP}) \cdot F_2^{IP}(\beta, Q^2)$, where $f_{IP}(x_{IP})$ is the flux of Pomerons in the proton, which can be extracted[82] from diffractive hadron-hadron scattering within an uncertainty of about 30%. Regge theory[83] predicts that if the $x_{IP}$ dependence corresponds to a flux of Pomerons associated with the proton, then $F_2^{D(3)} \propto 1/x_{IP}^n$, where $n = 2\alpha(t) - 1$, and $\alpha(t) = \alpha(0) + \alpha' t$ is the Pomeron trajectory. The first measurements of $F_2^{D(3)}$ by H1 (Ref. 84) and ZEUS[85] established the attribution of the rapidity gap events to a virtual photon-proton process that was dominantly diffractive. Figure 31 shows a recent measurement of $x_{IP} \cdot F_2^{D(3)}$ by H1 (Ref. 86) as a function of $x_{IP}$ for different

values of $\beta$ and $Q^2$. The data is compared to a fit of the form $(x_{IP})^{-n(\beta)}$ with the normalization in each bin determined by the factor $A(\beta, Q^2)$.
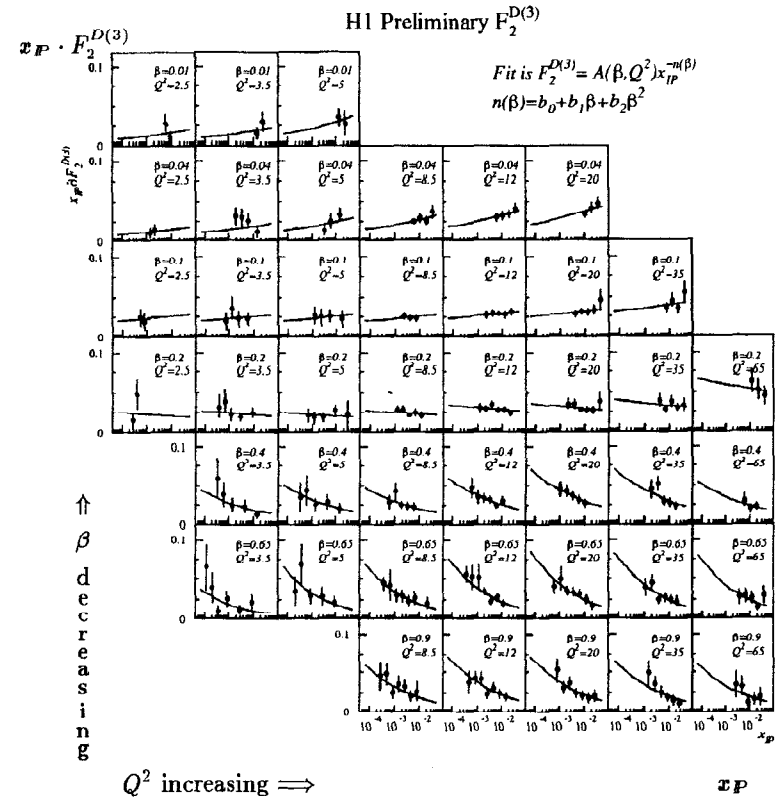


Figure 31. Preliminary measurement of $x_{IP} \cdot F_2^{D(3)}$ by H1 as a function of $x_{IP}$ in bins of $Q^2$ and $\beta$ with statistical and systematic errors added in quadrature. The curves are from the overall parameterization of the $x_{IP}$ dependence described in the text.

Figure 32(a) shows the H1 (Ref. 86) result from fitting the data of Figure 31 to the polynomial dependence $1/x_{IP}^n$, where $n$ is allowed to vary with $\beta$, but not with $Q^2$. The value of $n$ decreases markedly with $\beta$ for $\beta \leq 0.3$, which shows that the expectation of factorization of $F_2^{D(3)}$ is not valid over the full kinematic range. However, H1 note that these deviations from factorization are consistent with a contribution to $F_2^{D(3)}$ from meson exchange. An example of such a meson trajectory would be the $f_2^0(1270)$, which would have $n \sim 0$ and possibly a much softer $\beta$ dependence than the Pomeron

trajectory. Figure 32(b) shows the result where $n$ is allowed to vary with $Q^2$, but not with $\beta$. There is no evidence for dependence of $\beta$ on $Q^2$.
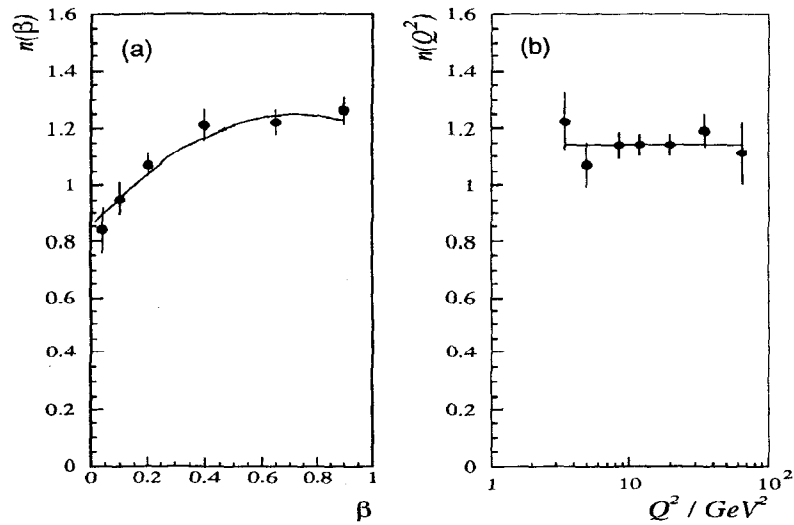


Figure 32. Preliminary H1 results from fitting $x_{IP} \cdot F_2^{D(3)}(\beta,Q^2,x_{IP})$ to the form $F_2^{D(3)} \propto 1/x_{IP}^n$. In (a), $n$ is allowed to vary with $\beta$, but not with $Q^2$. In (b), $n$ is allowed to vary with $Q^2$ but not with $\beta$. The error bars include statistical and systematic uncertainties folded in quadrature.

In spite of the lack of factorization of the measured diffractive cross section over the entire kinematic range, integrating over $x_{IP}$ produces a measurement of the average deep inelastic structure of the total colorless, isospin-conserving exchanges involved.
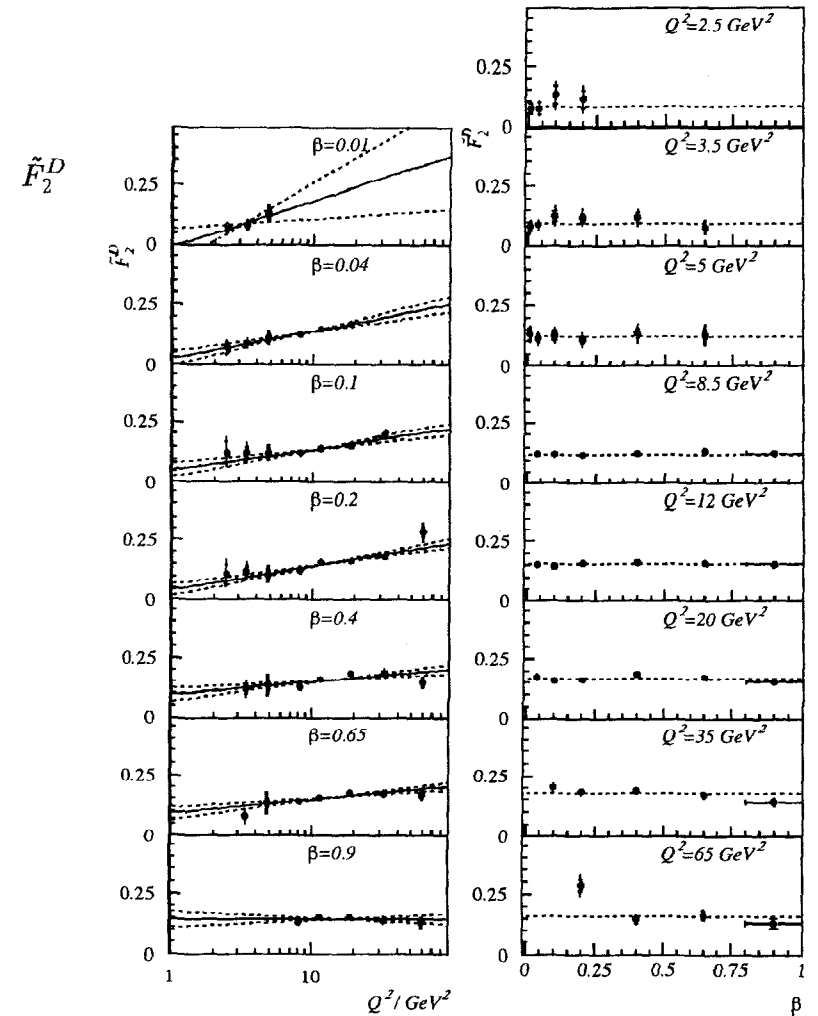


Figure 33. Preliminary measurement by H1 of $\tilde{F}_2^D(\beta,Q^2)$ as a function of $Q^2$ for different $\beta$ values (left) and as a function of $\beta$ for different $Q^2$ values (right). The solid lines in the $Q^2$ plots are the best fit to a linear dependence on $\ln Q^2$, with dashed lines at $\pm 1\sigma$. The dashed lines in the $\beta$ plots show a constant dependence on $\beta$.

H1 defines[86] $\tilde{F}_2^D(\beta,Q^2) = \int\limits_{x_{IP}=0.0003}^{x_{IP}=0.05} F_2^{D(3)}(\beta,Q^2,x_{IP})dx_{IP}$. Figure 33 shows $\tilde{F}_2^D(\beta,Q^2)$ from

H1 as a function of $Q^2$ for fixed $\beta$ and as a function of $\beta$ for fixed $Q^2$. At fixed $Q^2$,

$\tilde{F}_2^D(\beta, Q^2)$ shows little dependence on $\beta$. The dependence of $\tilde{F}_2^D(\beta, Q^2)$ on $Q^2$ shows clear evidence of scaling violation. Most notable is the persistence of the rise with $\ln Q^2$ that persists to values of $\beta$ beyond the point where the proton structure function is dominated by valence quarks ($x \sim 0.15$) and not by gluons. These scaling violations are in agreement with a picture where there is a substantial gluon contribution to the diffractive exchange. H1 have performed a QCD analysis of $\tilde{F}_2^D(\beta, Q^2)$ using DGLAP evolution and conclude that at $Q^2 = 5$ GeV$^2$, "leading" gluon behavior is seen, where the exchange is mostly taking place through gluons carrying a large ($> 0.9$) fraction of the Pomeron's momentum, and that throughout the observed $Q^2$ range from 5 to 65 GeV$^2$, more than 80% of the momentum transfer in the diffractive exchange is due to gluons, with a decreasing momentum fraction with increasing $Q^2$.

## 4.6. Diffraction with a Tagged Leading Proton

ZEUS has used its Leading Proton Spectrometer (LPS) to measure scattered protons with small transverse momenta ($p_T < 1$ GeV) with respect to the proton beam direction. The LPS provides a direct measurement of $x_L = p'/p_{beam}$ with 0.4% resolution[87] at $p_{beam} = 820$ GeV, as well as $x_{I\!P} \sim 1 - x_L$ and $t = -\frac{1}{x_L} p_T^2 + m_p^2 \frac{(1 - x_L)}{x_L}$. This provides the opportunity to directly measure $t$ with a resolution $\sim 30\%$, dominated by the transverse spread in the proton beam. The identification of single diffractive events (where the proton remains intact) by the presence of rapidity gaps results in considerable backgrounds from nondiffractive DIS of up to 50% and proton dissociation (where the proton does not remain intact) of 10–15% (estimated from hadron scattering data). Figure 34 shows the $x_L$ distribution for ZEUS data,[88] compared with MC calculations of events from diffraction (RAPGAP[89]) and the backgrounds from nondiffractive DIS, pion exchange, and proton dissociation. There is excellent agreement between the model and the data with a clear diffractive peak at high $x_L$. The backgrounds peak at low $x_L$ values. Therefore, the LPS enables the selection of a clean sample of diffractive events by requiring $x_L > 0.97$, with a uniform acceptance in $x_L$, after averaging over an azimuthal angle of 6%. The remaining background for $x_L > 0.97$ is estimated to be $\sim 5\%$ and is subtracted from the subsequent LPS results.
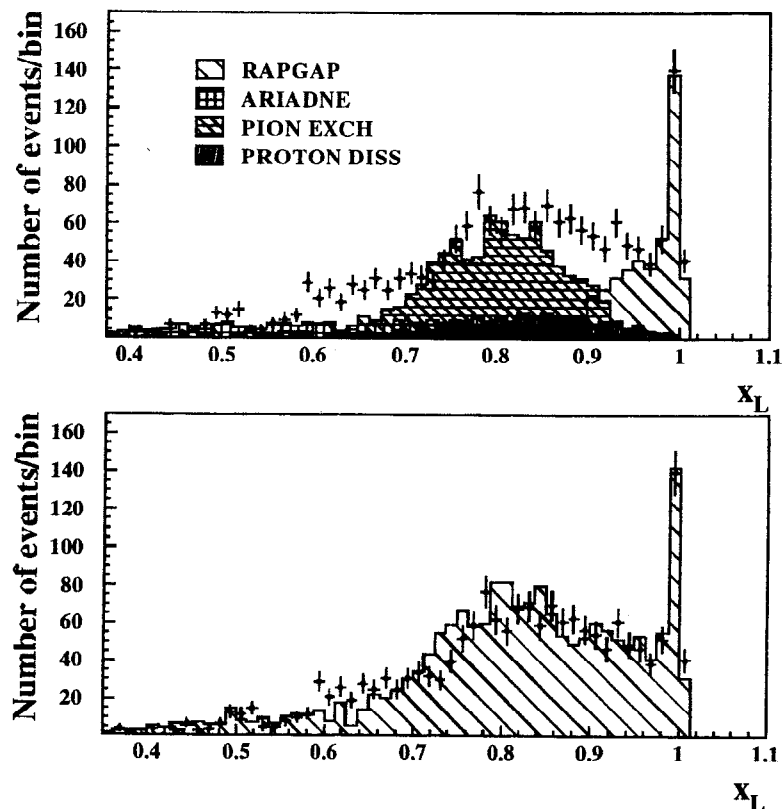


Figure 34. $x_L = p'/p_{beam}$ distribution for ZEUS data compared with individual (upper plot) and summed (lower plot) MC calculations of events from DIS (ARIADNE), pion exchange, proton dissociation, and diffraction (RAPGAP).

Figure 35 shows the ZEUS LPS measurement of the $t$-dependence of diffractive DIS events measured in the kinematic range $4 < Q^2 < 30$ GeV$^2$, $70 < W^2 < 210$ GeV$^2$, $0.02 < \beta < 0.4$, and $x_L > 0.97$. The bin width in $t$ was selected to be larger than the resolution, producing four bins in the range $0.07 < |t| < 0.35$ GeV$^2$. The distribution was fit to a single exponential of the form $d\sigma/d|t| \sim e^{-b|t|}$ and is shown in Figure 35 as a solid line. The value of the fitted slope parameter $b = 5.9 \pm 1.3(stat)^{+1.1}_{-0.7}(syst)$ GeV$^2$.
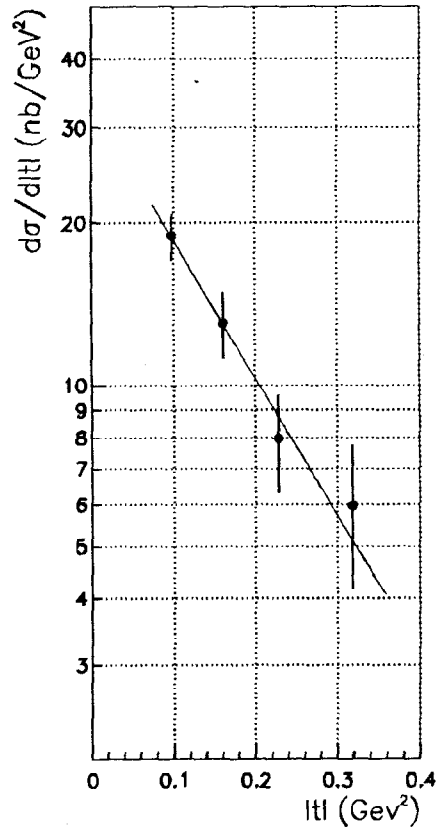
Figure 35. Differential cross section $d\sigma/d|t|$ from ZEUS for diffractive DIS events with a tagged leading proton having $x_L > 0.97$, along with an exponential fit described in the text. The error bars include statistical and systematic errors added in quadrature.

Figure 36 shows the ZEUS measurement[88] of the diffractive structure function, $F_2^{D(3)}(\beta, Q^2, x_{IP})$, integrated over $t$ due to the limited statistics, as a function of $x_{IP}$ in bins of $\beta$ for $0.006 < \beta < 0.5$, $4 \times 10^{-4} < x_t < 3 \times 10^{-2}$, and $4 < Q^2 < 20$ GeV$^2$ with a central value of $Q^2 = 12$ GeV$^2$. In order to investigate whether the factorization of $F_2^{D(3)}$ holds, fits were performed in the highest three $\beta$ bins to the form $A_i(1/x_{IP})^a$, where the normalization constants $A_i$ were allowed to vary in each bin. A very good fit is obtained ($\chi^2$ of 10 for 11 degrees of freedom) in all three $\beta$ bins with the value $a = 1.28 \pm 0.07$ (stat.) $\pm 0.15$ (syst.). Therefore, this result is compatible with factorization,

which is significant considering the removal of backgrounds, particularly that of meson exchange, that could affect the H1 result.
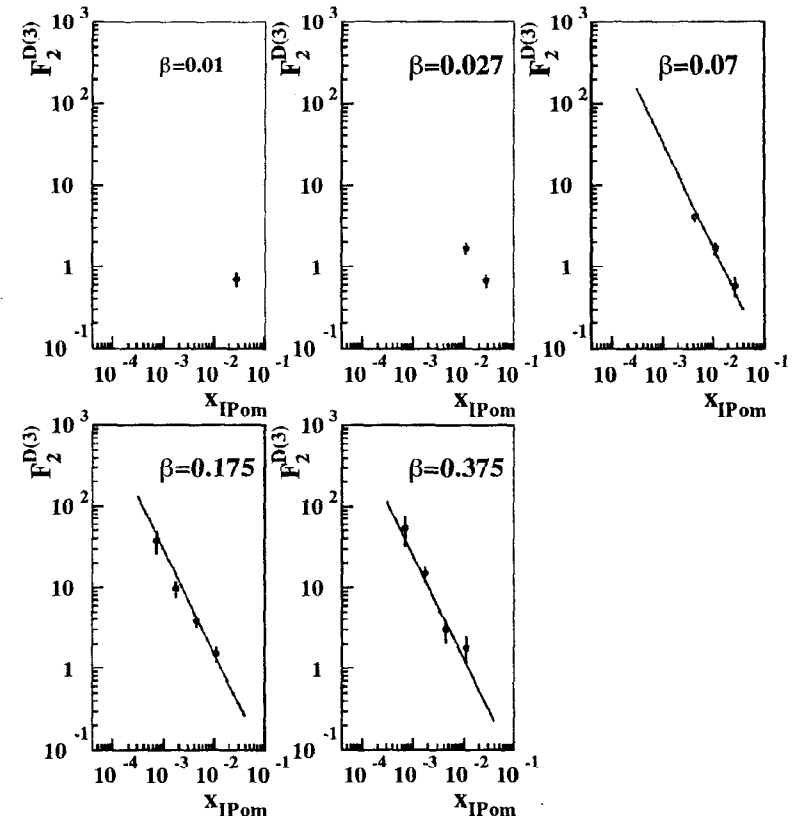


Figure 36. The diffractive structure function $F_2^{D(3)}(\beta, Q^2, x_{IP})$ from ZEUS, plotted as a function of $x_{IP}$ in five bins of $\beta$ at $Q^2 = 12$ GeV$^2$ compared with a fit described in the text. The errors are statistical only.

## 4.7. Diffractive Dijet Photoproduction

Diffractive hard photoproduction in $ep$ collisions occurs with $Q^2 \approx 0$ and a final state hadronic system containing at least one jet. ZEUS has examined dijet photoproduction events with a forward rapidity gap.[90] Figure 37(a) shows a schematic representation of such an event that proceeds via Pomeron exchange at small $t$. The indicator of the photon dissociation is the final state proton's retention of a large fraction of the original longitudinal momentum. A large rapidity gap between the hadronic system and the

scattered proton is produced by the exchange of a colorless object, *i.e.*, the Pomeron. The typical topology of a diffraction dijet photoproduction event is shown in Figure 37(b).
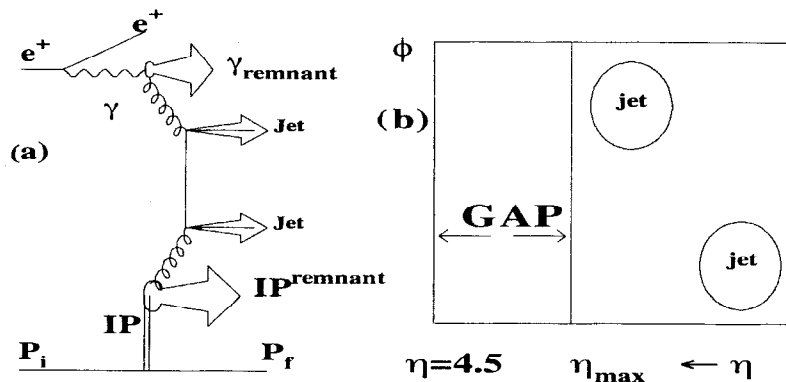


Figure 37. (a) Example of a two-jet diffractive process via Pomeron exchange at small $t$. (b) Typical topology of the event in (a) as seen by ZEUS.

ZEUS has measured[90] the dijet cross section for photoproduction events with the most forward-going hadron at $\eta < 1.8$, where the jets have $|\eta^{jet}| < 1.5$ and transverse energy, $E_t^{jet} > 6$ GeV, where $Q^2 < 4$ GeV$^2$ and $0.2 < E_\gamma/E_e < 0.8$, corresponding to photoproduction interactions with a center-of-mass energy in the range 134–269 GeV and a median $Q^2 \approx 10^{-3}$ GeV$^2$. This data has been compared with a factorizable Ingelman-Schlein (IS) model[91] where a parton from the Pomeron can directly scatter off the photon (direct photoproduction) or with a parton from the photon (resolved photoproduction). The flux of Pomerons in the proton is given by a parameterization of UA4 data.[92] A second model[93] from Donnachie and Landshoff (DL) calculates the Pomeron flux from fits to hadron-hadron data. The IS and DL Pomeron flux factors give similar results. ZEUS explored the effects of four different expressions for the density of partons in the Pomeron in terms of $\beta$, the momentum fraction of the struck parton in the Pomeron:

- super-hard gluon density: $\beta f_{g/IP}(\beta) = 0.1/(1-\beta)^{0.9}$ [similar to $\delta(1-\beta)$]
- hard gluon density: $\beta f_{g/IP}(\beta) = 6\beta(1-\beta)$
- soft gluon density: $\beta f_{g/IP}(\beta) = 6(1-\beta)^5$
- quark density (two flavors): $\beta f_{g/IP}(\beta) = 1.5\beta(1-\beta)$.

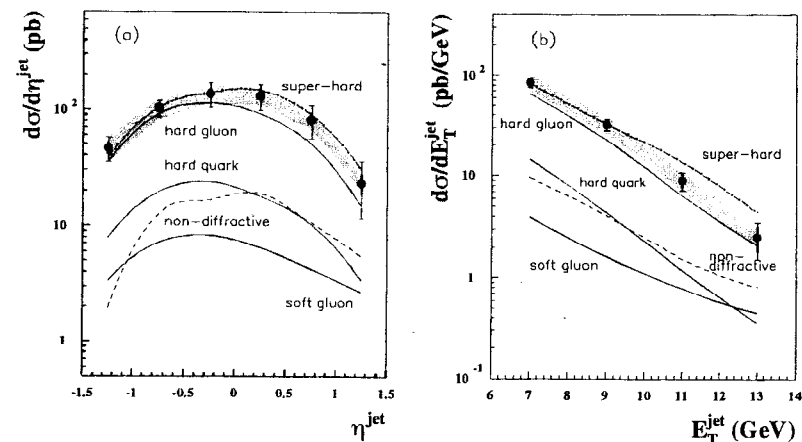These were implemented in the framework of the POMPYT[80] model.



Figure 38. ZEUS differential dijet photoproduction cross section as a function of (a) $\eta^{jet}$ and (b) $E_T^{jet}$. The thick error bars show the statistical error and the thin error bars show the statistical and systematic errors added in quadrature (excluding the jet energy scale error shown as a band). The data are compared with the POMPYT model using the inputs described in the text and with a calculation of the nondiffractive component.

The ZEUS-corrected differential dijet cross section $d\sigma/d\eta^{jet}$ with the cuts described above is shown in Figure 38(a). The cross section is flat in the central region and falls off as the jets approach the beam direction. The transverse energy differential cross section $d\sigma/dE_T^{jet}$ is shown in Figure 38(b). The cross section falls off exponentially as a function of $E_t^{jet}$. The figure shows that the expectation of the nondiffractive contribution caused by fluctuations in the final hadron system and estimated using PYTHIA including both direct and resolved, is three to eight times below the data for $d\sigma/dE_T^{jet}$ and seven times for $d\sigma/d\eta^{jet}$. Figure 38 also shows the diffractive model predictions using POMPYT, the DL Pomeron flux, and the parton distributions in the Pomeron listed above. The soft gluon density Pomeron parton distribution neither matches the data in shape nor normalization. The hard quark density describes the shape, but falls below the data. The hard and super-hard gluon densities provide reasonable descriptions of the data both in shape and magnitude.
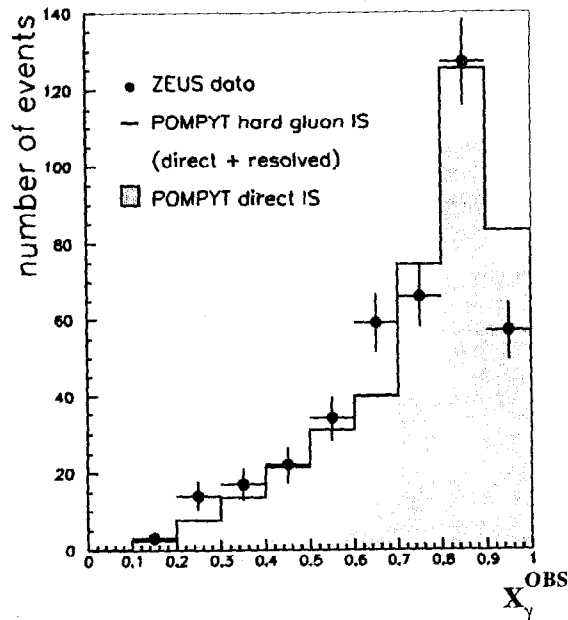
Figure 39. $x_\gamma^{OBS}$ distribution from ZEUS for diffractive photoproduction of dijets. The solid line shows POMPYT with resolved and direct contributions for a hard gluon density in the Pomeron. The direct contribution is shown as the shaded area.

Figure 39 shows the $x_\gamma^{OBS}$ distribution from ZEUS for diffractive photoproduction of dijets with the cuts described above. The $x_\gamma^{OBS}$ distribution peaks at $x_\gamma^{OBS} = 0.85$ with a large tail at low $x_\gamma^{OBS}$. The background from nondiffractive hard photoproduction, as calculated from PYTHIA, is estimated to be about $18 \pm 4$ % and is concentrated at large $x_\gamma^{OBS}$ values, so it cannot account for the amount of the data nor the low $x_\gamma^{OBS}$ tail. The dependence of the relative amounts of direct and resolved contributions to standard hard photoproduction is predicted to depend on the jet transverse energy.[94] The resolved contribution is expected to dominate over the direct in the $E_t^{jet}$ range of this sample. However, due to the limited center-of-mass energy, the direct contribution is expected to be enhanced.[90] Figure 39 shows that the sum of the direct and resolved contributions as predicted by POMPYT (histogram) with the hard gluon Pomeron parton density and IS Pomeron flux give a reasonable description of the data. In contrast, the prediction of the purely direct photoproduction contribution (shaded area) does not reproduce the data. This remains true when a hard quark density is used.

Therefore, one can conclude that resolved diffractive photoproduction is being observed.

## 5. Conclusions

The HERA collider and the H1 and ZEUS experiments have unearthed a rich source of information on the structure of the proton and the photon. The extension of the range of the proton structure function measurements by two orders of magnitude has uncovered the dramatic rise in $F_2$ with decreasing $x$ at low $Q^2$ that indicates a large increase in the gluon density. At low $Q^2$, we are observing the transition from perturbative QCD to the soft hadronic physics described by Regge theory. Studies of deep inelastic multijet events have shown the value and running of the strong coupling constant over a large $Q^2$ range within a single experiment. The observation of resolved and direct photoproduction, particularly in dijets, has provided new insight into the structure of the photon as well as the spin of the exchanged parton in these processes. The discovery of diffraction in $ep$ collisions both in deep inelastic scattering and in photoproduction has produced information about the structure of the Pomeron and the characteristics of the diffractive process.

The future for the HERA program looms particularly bright. While all of the above physics discussed in these lectures is based on data samples up through 1995 of around 10 pb$^{-1}$, the DESY Directorate has endorsed an upgrade plan for HERA that should yield luminosities of 150 pb$^{-1}$/year, with polarized electrons and positrons, beginning in the year 2000. Already, the 1996 run with positrons is expected to yield more than 10 pb$^{-1}$, with more improvements expected in 1997 and beyond, including switching to electrons in 1998. This large increase in luminosity should yield substantial physics results in all realms of HERA physics.[95] We can look forward to a much deeper understanding of the structure of the proton and photon, and maybe even some surprises.

# References

[1] E. Bloom et al., Phys. Rev. Lett. **23**, 930 (1968); M. Breidenbach et al., Phys. Rev. Lett. **23**, 935 (1968); R. Taylor, Rev. Mod. Phys. **63**, 573 (1991); H. Kendall, Rev. Mod. Phys. **63**, 597 (1991); J. Friedman, Rev. Mod. Phys. **63**, 615 (1991).

[2] J. D. Bjorken, Phys. Rev. **179**, 1547 (1969).

[3] R. P. Feynman, Phys. Rev. Lett. **23**, 1415 (1969).

[4] J. D. Bjorken and E. A. Paschos, Phys. Rev. **185**, 1975 (1969).

[5] J. Friedman et al., Phys. Rev. D **5**, 528 (1972).

[6] J. Kuti and V. F. Weisskopf, Phys. Rev. D **4**, 3418 (1971).

[7] V. N. Gribov and L. N. Lipatov, Sov. J. Nucl. Phys. **15**, 438 (1972); L. N. Lipatov, Sov. J. Nucl. Phys. **20**, 94 (1975); G. Altarelli and G. Parisi, Nucl. Phys. B **126**, 298 (1977).

[8] A. D. Martin, R. G. Roberts, and W. J. Stirling, Phys. Lett. B **354**, 155 (1995).

[9] R. Brock et al., Rev. Mod. Phys. **67**, 157 (1995).

[10] M. Glück, E. Reya, and A. Vogt, Z. Phys. C **65**, 157 (1995).

[11] A. Donnachie and P. V. Landshoff, Nucl. Phys. B **244**, 322 (1984); Phys. Lett. B **296**, 227 (1992); Phys. Lett. C **61**, 139 (1994).

[12] Y. Balitsky and L. Lipatov, Sov. J. Nucl. Phys. **28**, 822 (1978); E. Kuraev, L. Lipatov, and V. Fadin, Sov. Phys. JETP **44**, 443 (1976); Sov. Phys. JETP **45**, 443 (1977).

[13] T. Ahmed et al., Nucl. Phys. B **349**, 471 (1995).

[14] M. Derrick et al., Z. Phys. C **69**, 607 (1996).

[15] A. C. Benvenuti et al., Phys. Lett. B **223**, 485 (1989).

[16] M. Arneodo et al., Phys. Lett. B **364**, 107 (1995).

[17] M. R. Adams et al., Phys. Rev. D **54**, 3006 (1996).

[18] H. L. Lai et al., Phys. Rev. D **51**, 4768 (1996).

[19] A. D. Martin et al., Phys. Lett. B **387**, 419 (1996).

[20] S. Aid et al., Nucl. Phys. B **470**, 3 (1996).

[21] M. Derrick et al., DESY 96-076, accepted by Z. Phys. (1996).

[22] M. Derrick et al., Z. Phys. C **63**, 391 (1994).

[23] S. Aid et al., Z. Phys. C **69**, 27 (1995).

[24] D. O. Caldwell et al., Phys. Rev. Lett. **40**, 1222 (1978).

[25] H1 Collaboration, contributed paper PA02-70 to the 1996 International Conference on High Energy Physics, Warsaw, July 1996.

[26] S. Aid et al., Phys. Lett. B **379**, 319 (1996); S. Aid et al., Z. Phys. C **67**, 565 (1995); T. Ahmed et al., Phys. Lett. B **324**, 241 (1994).

[27] M. Derrick et al., Phys. Rev. Lett. **75**, 1006 (1995).

[28] L. Montanet et al., Phys. Rev. D **50**, 1173 (1994).

[29] S. Magill, ZEUS Note 94-154.

[30] T. Ahmed et al., Phys. Lett. B **346**, 415 (1995).

[31] M. Derrick et al., Phys. Lett. B **363**, 201 (1995).

[32] W. Bartel et al., Z. Phys. C **33**, 23 (1986); S. Bethke et al., Phys. Lett. B **213**, 235 (1988).

[33] T. Brodkorb et al., Z. Phys. C **44**, 415 (1989); D. Graudenz and N. Magnussen, Proceedings of the HERA Workshop 1991, DESY.

[34] T. Brodkorb and E. Mirkes, U. Wisconsin preprint MAD-PH-821, April 1994.

[35] D. Graudenz, Comp. Phys. Commun. **92**, 65 (1995).

[36] G. Ingelman and J. Rathsman, Z. Phys. C **59**, 213 (1994).

[37] E. Laenen et al., Nucl. Phys. B **392**, 228 (1993); S. Riemersma, J. Smith, and W. L. van Neervan, Phys. Lett. B **347**, 143 (1995); M. Glück, E. Reya, and M. Stratmann, Nucl. Phys. B **422**, 37 (1994).

[38] T. Trefzger, ZEUS Note 96-075.

[39] J. F. Owens, Phys. Rev. D **21**, 54 (1980); M. Drees and F. Halzen, Phys. Rev. Lett. **61**, 275 (1988); M. Drees and R. M. Godbole, Phys. Rev. D **39**, 169 (1989); G. A. Schuler and T. Sjostrand, Phys. Lett. B **300**, 169 (1993).

[40] J. J. Sakurai, Phys. Rev. Lett. **22**, 981 (1969).

[41] M. Derrick et al., Phys. Lett. B **348**, 665 (1995).

[42] T. Sjostrand and M. van Zijl, Phys. Rev. D **36**, 2019 (1987).

[43] S. D. Ellis, *Proceedings of the 28th Rencontre de Moriond*, 235 (1993).

[44] T. Ahmed *et al.*, Nucl. Phys. B **445**, 195 (1995).

[45] G. Schuler and T. Sjostrand, Nucl. Phys. B **407**, 539 (1993).

[46] ZEUS Collaboration, contributed paper pa02-040, *International Conference on High Energy Physics*, Warsaw, Poland, July 1996.

[47] G. Marchesini *et al.*, Comp. Phys. Comm. **67**, 465 (1992).

[48] J. M. Butterworth and J. R. Forshaw, J. Phys. G **19**, 1657 (1993).

[49] S. Aid *et al.*, Z. Phys. C **70**, 17 (1996).

[50] M. Derrick *et al.*, Phys. Lett. B **342**, 417 (1995).

[51] ZEUS Collaboration, contributed paper pa02-041, *International Conference on High Energy Physics*, Warsaw, Poland, July 1996.

[52] C. Albajar *et al.*, Nucl. Phys. B **309**, 405 (1988).

[53] T. Sjostrand, Comput. Phys. Comm. **82**, 74 (1994).

[54] R. Engel, Z. Phys. C **66**, 203 (1995).

[55] J. R. Forshaw and R. G. Roberts, Phys. Lett. B **319**, 539 (1993).

[56] ZEUS Collaboration, contributed paper pa02-040, *International Conference on High Energy Physics*, Warsaw, Poland, July 1996.

[57] J. Huth *et al.*, *Proceedings of the 1990 DPF Summer Study on High Energy Physics* (World Scientific, Singapore, 1992), p. 134; G. Arnison *et al.*, Phys. Lett. B **123**, 115 (1983).

[58] S. Catani, Y. L. Dokshitzer, M. H. Seymour, and B. R. Webber, Nucl. Phys. B **406**, 187 (1993).

[59] S. D. Ellis and D. E. Soper, Phys. Rev. D **48**, 3160 (1993).

[60] M. Glück, E. Reya, and A. Vogt, Phys. Rev. D **46**, 1973 (1992).

[61] J. Huston *et al.*, Phys. Rev. D **51**, 6139 (1995).

[62] S. D. Ellis, Z. Kunszt, and D. E. Soper, Phys. Rev. Lett. **69**, 3615 (1992).

[63] H. Baer, J. Ohnemus, and J. F. Owens, Phys. Rev. D **40**, 2844 (1989).

[64] M. Derrick *et al.*, Phys. Lett. B **384**, 401 (1996).

[65] J. Botts *et al.*, Phys. Lett. B **304**, 15 (1993).

[66] A. Martin, W. J. Stirling, and R. G. Roberts, Phys. Rev. D **50**, 6734 (1994).

[67] D. Perkins, *Introduction to High Energy Physics* (J. Wiley, 1988).

[68] M. Froissart, Phys. Rev. **123**, 1053 (1961).

[69] T. Regge, Nuovo Cimento **16**, 951 (1959); Nuovo Cimento **18**, 947 (1960).

[70] G. F. Chew and S. C. Frautschi, Phys. Rev. Lett. **7**, 394 (1961) and **8**, 41 (1962).

[71] A good review is found in *Regge Theory of Low-$p_T$ Interactions*, edited by L. Caneschi (North-Holland, 1989).

[72] A. Donnachie and P. V. Landshoff, Phys. Lett. B **296**, 227 (1992).

[73] Particle Data Group, Phys. Rev. D **54**, 191 (1966).

[74] M. Bozzo *et al.*, Phys. Lett. B **136**, 217 (1984).

[75] G. Ingelman and P. E. Schlein, Phys. Lett. B **152**, 256 (1985).

[76] R. Bonino *et al.*, Phys. Lett. B **211**, 239 (1988).

[77] A. Brandt *et al.*, Phys. Lett. B **297**, 417 (1992).

[78] M. Derrick *et al.*, Phys. Lett. B **316**, 207 (1993).

[79] A. DeRoeck, *Proceedings of the 1993 EPS Conference*, Marseille, DESY 94-005; J. Dainton, *Proceedings of the 1993 Lepton-Photon Conference*, Cornell.

[80] P. Bruni and G. Ingelman, *Proceedings of the 1993 EPS Conference*, Marseille, 595, DESY 93-187.

[81] G. Ingelman and K. Jansen-Prytz, Z. Phys. C **58**, 285 (1993).

[82] K. Prytz, Z. Phys. C **64**, 79 (1994).

[83] P. D. B. Collins, *An Introduction to Regge Theory and High Energy Physics* (Cambridge University Press, 1977) p. 418.

[84] T. Ahmed *et al.*, Phys. Lett. B **348**, 681 (1995).

[85] M. Derrick *et al.*, Z. Phys. C **68**, 569 (1995).

[86] H1 Collaboration, contributed paper pa02-061, 1996 Lepton-Photon Conference, Warsaw.

[87] ZEUS Collaboration, contributed paper pa02-050, 1996 Lepton-Photon Conference, Warsaw.

[88] ZEUS Collaboration, contributed paper pa02-026, 1996 Lepton-Photon Conference, Warsaw.

[89] H. Jung, DESY preprint DESY93-182.

[90] ZEUS Collaboration, contributed paper pa02-039, 1996 Lepton-Photon Conference, Warsaw.

[91] P. Bruni and G. Ingelman, *Proceedings of the International Europhysics Conference*, Marseille, France, 1993.

[92] M. Bozzo *et al.*, Phys. Lett. B**136**, 217 (1984).

[93] A. Donnachie and P. V. Landshoff, Nucl. Phys. B **303**, 634 (1988); Phys. Lett. B **285**, 172 (1992).

[94] Drees and Grassie, Z. Phys. C **28**, 451 (1985).

*[95] Proceedings of the Workshop on Future Physics at HERA*, edited by G. Ingelman, A. De Roeck, and R. Klanner, DESY Report (http://www.desy.de/~heraws96), 1996.